Automation in Construction 182 (2026) 106750

Contents lists available at ScienceDirect

Automation in Construction

journal homepage: www.elsevier.com/locate/autcon

AI-driven conceptual optimization of building façade layouts using a fuzzy-logic-based morphological index

Carlotta Pia Contiguglia [a], Giuseppe Quaranta [b], Cristoforo Demartino [a,*], Billie F. Spencer Jr [c]

[a] Department of Architecture, Roma Tre University, Largo G. B. Marzi 10, 00153 Rome, Italy
[b] Department of Structural and Geotechnical Engineering, Sapienza University of Rome, Via Eudossiana 18, 00184 Rome, Italy
[c] Department of Civil and Environmental Engineering, University of Illinois Urbana-Champaign, IL, USA

ARTICLE INFO

Keywords:
Building façade
Conceptual design
Fuzzy logic
Fuzzy inference system
Morphology
Optimization

ABSTRACT

This paper introduces a computational framework that bridges the gap between qualitatively driven architectural intent and quantitatively grounded engineering optimization in the context of building façade design. At the core of the framework is a Morphological Index (MI) based on fuzzy inference, which synthesizes measurable attributes of the façade layout into a single, interpretable score. This index, in turn, serves as the objective of an optimization algorithm tasked with shaping the façade's morphology according to designers' preferences. A series of numerical investigations illustrates the framework's adaptability to diverse morphological design goals. Ultimately, the conversion of optimized layouts into expressive representations via artificial-intelligence-powered visualizations confirms the framework's applicability to automated conceptual design of building façades.

1. Introduction

This section provides an overview of the study's conceptual framework and structure. It presents the building façade as a system in which morphological factors remain challenging to integrate into automated design processes (Section 1.1). Section 1.2 discusses the suggested framework and introduces how subjective architectural intent is integrated into a optimization procedure.

1.1. Motivation

The façade[1] of a building is more than just its outer skin; it serves as the interface between interior spaces and the surrounding context. It is essential in defining the building's aesthetics[2] [5] while also influencing its structural behavior [6], acoustic [7], thermal and daylight performance [6,8,9], as well as its environmental impact [8,10]. Morphology[3] also plays a fundamental role, encompassing the arrangement, shape, and relative positioning of components such as walls, windows, balconies, loggias, and decorative elements [11,12]. A significant distinction exists, however, between morphology and other façade properties. In fact, façade characteristics such as structural behavior, acoustic insulation, thermal and daylight performance, and environmental impact can be relatively easily quantified. This quantifiability enables their direct integration into automated design processes and optimization problems. Morphology, however, still lacks a quantifiable measure. This makes it challenging to formalize and incorporate morphological aspects as a singular metric within algorithmic design workflows. As a result, the morphological aspect of façades is often modeled indirectly or treated qualitatively a posteriori, thereby limiting the holistic consideration of design alternatives within automated design procedures.

To address this gap, the present study adopts a perspective grounded in Human–Computer Co-Creativity (HC^3), following Hoffmann's view of computational systems as creative partners capable of expanding the design space, evaluating design alternatives, and supporting communication within the design workflow [13]. Building on these principles, we introduce a fuzzy-logic-based method that embeds subjective architectural intent directly within automated façade optimization. A Fuzzy

---

* Corresponding author.
E-mail addresses: carlottapia.contiguglia@uniroma3.it (C.P. Contiguglia), giuseppe.quaranta@uniroma1.it (G. Quaranta), cristoforo.demartino@uniroma3.it (C. Demartino), bfs@illinois.edu (B.F. Spencer Jr).

[1] The term "façade" originates from the French word for "frontage" or "face" [1,2]. The term "façade" is derived from the Vulgar Latin term "facies" or "facia", meaning "front" or "face", which corresponds to the English term "appearance" [3].

[2] Aesthetics pertains to the visual perception of the façade. It encompasses the subjective qualities that make a building façade visually appealing.

[3] The word "morphology" is derived from the Greek terms μορφή (morph), meaning "form", and λογία (-ology), which refers to "treatise", "study", or "science" [4]. It denotes the physical form and structure of the façade, encompassing the arrangement of its elements and its geometric properties.

https://doi.org/10.1016/j.autcon.2025.106750
Received 21 July 2025; Received in revised form 23 December 2025; Accepted 27 December 2025

Nomenclature

N	Number of storeys in the façade grid
M	Number of bays in the façade grid
$\mathbf{F}$	Block matrix representing the entire façade layout
$\mathbf{f}_{i,j}$	Block matrix of attributes for the field at storey i and bay j
H_i, L_j	Height of the ith storey and length of the jth bay
$\mathcal{T}$	The complete inventory of available wall types
T	Total number of unique wall types in the inventory $\mathcal{T}$
$t_{i,j}$	Integer identifier for the wall type at field (i,j)
$A_{i,j}$	Area of the façade field at position (i,j)
$flip_{\mathrm{V}}(t)$	Function mapping wall type t to its vertically reflected counterpart
$flip_{\mathrm{H}}(t)$	Function mapping wall type t to its horizontally reflected counterpart
MI	Morphological Index (i.e., the final aggregated score for façade morphology)
m	Generic morphological metric
m_B	Balance metric
m_C	Continuity metric
m_D	Density metric
m_E	Edge Density metric
m_G	Ground Floor Density metric
m_P	Pattern metric
m_R	Rhythm metric
m_{S_V}	Vertical Symmetry metric
m_{S_H}	Horizontal Symmetry metric
m_U	Uniformity metric
$\mathcal{M}$	Fuzzy set representing a qualitative category (e.g., ‘high’, ‘low’)
$\mu_{\mathcal{M}}(m)$	Membership Function for metric m in set $\mathcal{M}$
Ω_m	The universe of discourse for a metric m
t, s	Triangular norm (t-norm) and co-norm (s-norm) for fuzzy logic
$\mathbf{x}$	Design vector containing the wall type identifiers for all fields
$f_{obj,r}$	The rth objective function
ω_r	Weight assigned to the rth objective function
$E_{raw}(\mathbf{x})$	Raw (un-normalized) value of embodied carbon
$e_{i,j}$	Unit value of embodied carbon for the wall type at field (i,j)
$e_{\mathrm{glass}}, e_{\mathrm{CLT}}$	Unit embodied carbon for glass and CLT
p_c, p_m	Crossover and mutation probabilities in the Genetic Algorithm
η	Distribution index for polynomial mutation in the Genetic Algorithm
$\rho(i,j)$	Transparency level of field (i,j), ranging from 0 (transparent) to 1 (opaque)
σ, μ	Standard deviation and mean, respectively
B_L, B_R	Parameters for left and right halves of the façade in the Balance metric
$c_t(w)$	Counting function for sub-patterns of type t and size w
DFS	Depth-First Search algorithm used for the Continuity metric
$V(i,j)$	Binary flag indicating if field (i,j) has been visited in DFS
F_{max}	Total number of filled (non-empty) fields in the façade
P_{max}	Size of the dominant sub-pattern in the façade
S_{max}	Size of the largest connected path of fields
$\mathcal{W}$	The set of all sliding window sizes for pattern detection
w_H, w_L	Height and width of the sliding window in the pattern metric

Inference System (FIS) is used to translate designers’ linguistic preferences into a single evaluative score — the Morphological Index (MI) — which aggregates multiple morphological attributes into a unified measure. This score becomes the objective guiding the optimization of façade layouts. By allowing designers to express qualitative judgments through linguistic rules that explicitly steer the search, the framework permits solutions to be informed both by performance targets and by creative insight. Through extensive numerical investigations, we demonstrate that this approach empowers designers to explore innovative, high-performance solutions that also align with their architectural vision.

1.2. Outline and proposed framework

Fig. 1 schematically illustrates the proposed framework for the automatic conceptual optimization of building façade morphology, with the paradigm shift it introduces highlighted through comparison with the state-of-the-art review in Section 2. Section 3 elaborates on the methodology introduced above. Section 4 then demonstrates its application through a series of numerical investigations of increasing complexity, followed by Section 5, which reports and discusses the corresponding results. Finally, Section 6 summarizes the key findings, discusses the main limitations, and outlines potential directions for future research.

The workflow of the proposed framework, based on the concept of fuzziness (Section 3.1), begins with the definition of the inputs (1), where the designer specifies the geometry of the façade and the inventory of available wall types (Section 3.2). A set of morphological metrics (Section 3.3, with detailed formulations in Appendix A) is computed to describe the façade composition quantitatively. In the next stage (2), the FIS processes the computed metrics using a knowledge base that contains designer-defined qualitative rules and associated fuzzy sets (Section 3.4). This stage translates quantitative metric values into linguistic assessments, combining them through fuzzy reasoning to produce a single crisp output (i.e., the MI). The MI serves as the objective function for the design optimization carried out via a Genetic Algorithm (GA) in the following stage. During the optimization stage (3), the GA evaluates each candidate solution based on its corresponding MI value, applies genetic operators to generate new configurations, and iteratively evolves the population until a termination criterion is reached (Section 3.5). In the final stage (4), the optimized façade layouts are presented to the designer for final selection, ensuring that creative and critical judgment remain central to the process (Section 3.6). The selected design is subsequently subjected to automated rendering through AI algorithms for refinement and visual presentation.

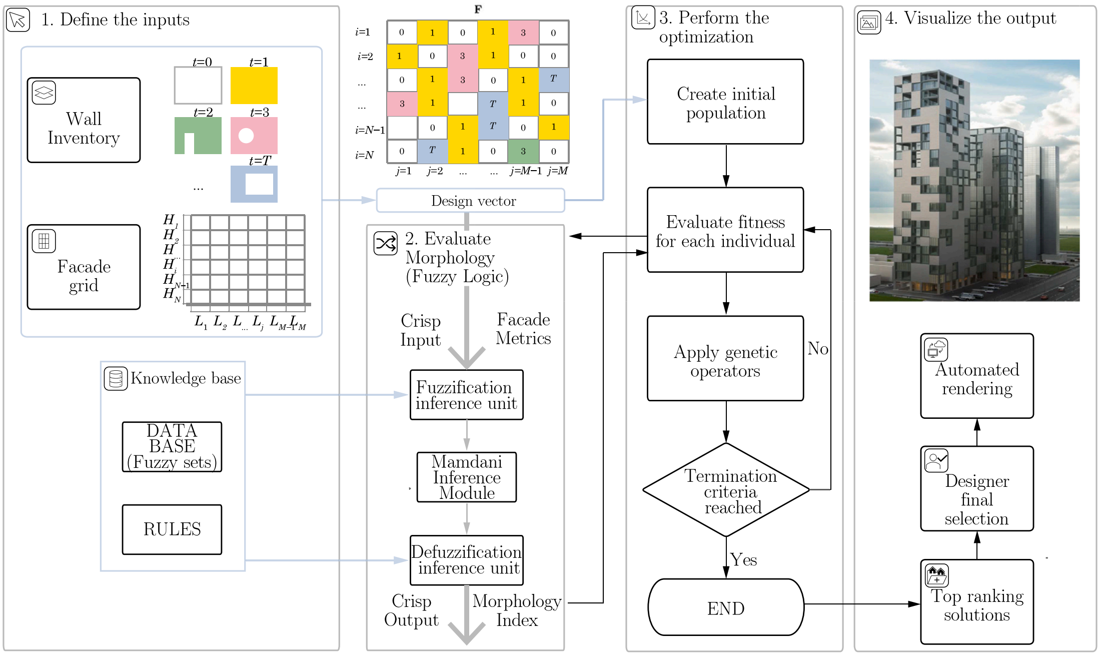

Fig. 1. Workflow of the proposed design framework for automatic conceptual optimization of the building façade.

2. Related work

A critical review of previous research provides insight into how morphology is typically addressed in building façade design and elucidates the dichotomy between morphological aspects and other façade characteristics with respect to their quantifiability, thereby uncovering how this divergence influences the advancement of holistic automated design methodologies.

Digitalization has increasingly shaped the way façade morphology is conceived and developed. Early parametric modeling approaches demonstrated the capability of digital tools to generate large sets of alternative façade solutions rapidly [14,15]. For instance, Rapone and Saro [16] and Bao et al. [17] showed how parametric procedures and procedural modeling can create systematic façade variations, while Moghtadernejad et al. [2] highlighted the role of digital workflows in accelerating exploratory design.

Multi-objective optimization (MOO) has become a dominant paradigm for façade design decisions. A chronological trend analysis by Shan and Junghans [18] shows that the number of studies on façade optimization has grown exponentially: early research focused mainly on energy performance [19,20], whereas more recent studies increasingly include cost [21,22], daylight [23,24], and thermal comfort [25,26]. Environmental and sustainability criteria are also emerging, although still underrepresented. Despite this evolution, most of these contributions treat morphology as a secondary effect of performance-oriented optimization rather than as a first-class design objective.

Some early studies have attempted to formalize morphological intent within computational workflows. Pugnale and Sassone [27] explored the use of evolutionary algorithms to generate and optimize free-form shell geometries, highlighting the role of the designer as a decision-maker within multi-objective trade-offs. Gaspar-Cunha et al. [28] proposed an interactive multi-objective optimization strategy to incorporate aesthetic criteria — typically non-quantifiable — into the search process, expanding the range of designer-relevant solutions. Similarly, Byrne et al. [29] developed an evolutionary framework in which structural constraints guide the exploration of conceptual forms originally shaped by aesthetic rules. Despite these advances, comprehensive reviews [30–35] consistently report that façade geometry remains rarely treated as an explicit, quantifiable design objective, and typically emerges only as a byproduct of performance-driven optimization.

Parallel to optimization research, automated façade generation using AI has gained attention. Techniques employing generative adversarial networks, variational autoencoders, and diffusion models have been proposed for façade synthesis or stylistic translation. For instance, Kuang et al. [12] demonstrated the use of diffusion models for reconstructing historical façades, while the reviews by Duran et al. [36] and Li et al. [37] comprehensively examined how AI-driven generative tools are currently applied in architectural workflows. However, as clarified by Duran et al. [36], most AI-based façade generation remains image-oriented and cannot yet be integrated into parametric or optimization pipelines due to the absence of a quantifiable morphological descriptor.

Some recent studies have explicitly aimed to incorporate designer preference or aesthetic intent into algorithmic processes. Yi [24] introduced an inference engine to embed façade appearance preferences alongside daylight criteria within a MOO setting. Ochoa et al. [38] merged combinatorial equilibrium models with machine-learning classification to learn aesthetic preferences, while Guo et al. [39] used natural language processing to translate semantic input into structured morphological configurations. These contributions mark significant steps toward capturing architectural intent computationally, though they stop short of defining a generalized, quantifiable measure of façade morphology. This gap represents the key constraint in the explicit integration of morphology into conceptual optimum façade design.

3. Methodology

This section describes the proposed framework's components and how they operate together within an integrated workflow. It provides a conceptual foundation for transforming qualitative morphological intent into a measurable objective using fuzzy sets and fuzzy inference (Section 3.1). It then formalizes the façade representation and wall inventory (Section 3.2), presents the morphological metrics used as inputs (Section 3.3), and explains how the morphological index (Section 3.4) is implemented in an optimization procedure (Section 3.5). Finally, it describes the AI-based visualization process that translates optimum layouts into design renderings (Section 3.6).

3.1. Conceptual basis

This study introduces the MI as a fundamental tool for assessing how effectively a façade fulfills the designer's morphological intent and, ultimately, for identifying configurations that are morphologically consistent with the designer's vision within an optimization-based parametric design exploration process. The MI is formulated to account for the relevant morphological aspects of the façade. In doing so, the MI is designed to bridge the gap between subjective morphological preferences regarding façade appearance and objective design parameters, fostering the development of automated tools that closely reflect expert knowledge.

In principle, the MI can be assessed using classical logic, which employs a binary approach to evaluate the degree to which design criteria are fulfilled. In this approach, a layout that fully complies with a certain design criterion is assigned a value of 1, while a noncompliant layout is given a value of 0. These values represent the degree of membership in a classical (or crisp) set, indicating complete inclusion (1) or complete exclusion (0) [40]. Taking vertical symmetry as an example of morphological feature, Fig. 2(a) illustrates that, out of three alternative façade layouts, two do not strictly meet the requirement (i.e., have a degree of membership of 0 in the target design criterion), while only one is fully compliant, with an associated degree of membership of 1. Although straightforward, the binary approach is limited by its rigidity, often conflicting with the subjective nature of morphological criteria and, ultimately, with the human-based reasoning process implemented in building façade design. Layouts that partially fulfill a design criterion can still be valuable, especially when multiple objectives must be balanced, even if they are not as preferable as fully compliant solutions. Furthermore, as the design process involves refining initially non-compliant solutions to accommodate multiple preferences, rejecting all unfeasible layouts during the exploratory stage would limit the effectiveness of automated design processes. Therefore, this study proposes a flexible approach using fuzzy sets and fuzzy logic to evaluate façade morphology, which better supports the automatic exploration of optimal configurations [41–43]. While fuzzy logic has been previously applied to spatial analysis [44] and aesthetic evaluation [45], its potential as a core component of design optimization remains underexplored.

Unlike the rigid binary approach, fuzzy sets enable a graduated evaluation of how well a design criterion is met. A fuzzy set allows elements to have partial degrees of membership, typically represented by a value between 0 (no membership) and 1 (full membership) [43,46]. This degree of membership is quantified by a membership function, which maps each element of the universe of discourse (the range of possible values for a variable) to a real number in the interval [0, 1]. In Fig. 2, three alternative layouts are considered, differing in the degree to which they meet the morphological feature (moving from left to right: very low vertical symmetry, medium vertical symmetry, and high vertical symmetry). Fig. 2(a) demonstrates a binary evaluation, where the layout is either fully compliant (output equal to 1) or non-compliant (output equal to 0). Fig. 2(b) uses a continuous approach, assigning intermediate values between 0 and 1 based on the level of symmetry. The three representative façade layouts are then assessed based on how well the design criterion related to vertical symmetry is fulfilled, closely mimicking a human-based evaluation and facilitating their proper consideration throughout the design process. Beyond individual criteria, fuzzy logic further enables the modeling of the complex interdependencies among multiple morphological features, enabling the conversion of the typical evaluation process driven by expert judgments into automated design procedures.

3.2. Façade definition and wall inventory

The implementation of the proposed MI requires a formal definition of the building façade. In the context of the present study, a planar façade consisting of $N \times M$ square or rectangular fields is considered, as shown in Fig. 3.

This façade is intended to represent a typical multi-storey building exterior. The height and length of each field composing the façade are denoted as H_i and L_j, respectively, where $i = 1, \ldots, N$ and $j = 1, \ldots, M$. The façade is fully characterized by a block matrix $\mathbf{F}$, where each block $\mathbf{f}_{i,j}$ collects relevant attributes for the (i, j)th field. In this study, a limited set of attributes is considered for each field, such that $\mathbf{f}_{i,j} = \begin{bmatrix} H_i & L_j & t_{i,j} & e_{i,j} \end{bmatrix}$, where $t_{i,j}$ represents the wall type of the (i, j)th field and can take any value from the wall inventory $\mathcal{T} = \{t\} = \begin{Bmatrix} 0 & 1 & \cdots & T \end{Bmatrix} \subset \mathbb{N}$. Without loss of generality, $t_{i,j} = 0$ corresponds to a field without a wall, $t_{i,j} = 1$ represents a solid wall, and $t_{i,j} = 2, \ldots, T$ denotes walls with openings of different geometries and/or positions (the number of wall types is thus equal to T). Moreover, $e_{i,j}$ represents the unit value of the embodied carbon dioxide equivalent of the (i, j)th field, which is determined by materials and geometric configuration of the specific wall type $t_{i,j}$. Furthermore, this wall inventory $\mathcal{T}$ is a highly extensible input that is completely user-defined and problem-based. Instead of being limited by a predetermined set, designers are free to create any number of unique wall types, each with a variety of features pertaining to geometry (both in plan and out of plane), material, particular functions, shading characteristics, and other performance-related factors.

3.3. Morphological metrics

The visual and spatial organization of the façade is often determined not by a single feature but by multiple, possibly conflicting aspects. As evaluating all relevant features is essential for automatically designing the façade morphology, a set of metrics is proposed in Table 1, focusing on key aspects of the façade morphology. For visual interpretation, see the illustrative examples of façade layouts in Fig. 4, which correspond to high values for each morphological metric.

The generic metric, denoted as m, quantifies a specific morphological aspect of the façade based on its characteristics, which are collected in $\mathbf{F}$. The detailed mathematical formulation for each metric can be found in Appendix A. A concise description of each metric is also reported in Table 1, highlighting the specific façade characteristic it measures. Although not exhaustive, these metrics capture key visual and spatial characteristics that are influential in the design process of façades. As for the wall inventory, the specification of metrics is a highly expandable input that is completely user-defined and problem-based. Additionally, the framework supports the construction of customized metrics that go beyond the morphological features shown in Table 1. This versatility makes it possible to create metrics that are sensitive to aspects like a building's functional program or the morphological effects of 3D element combinations, where spatial linkages and volumetric interactions are crucial.

Fig. 4 also presents illustrative examples of façade layouts that rank among the best according to each of the morphological metrics described in Table 1, facilitating their interpretation. In the example relative to m_U, the red numbers to the left and on the bottom indicate how many fields are filled in the corresponding row or column. Dashed red lines highlight the axis used to calculate the symmetry for some metrics, such as m_{SV} and m_{SH}, or specific areas related to the calculation of other metrics like m_C, m_R, and m_E.

When combined, these metrics allow for the efficient measurement of the façade's many visual and spatial characteristics and empower designers to optimize their designs for solutions that are both visually appealing and functionally viable.

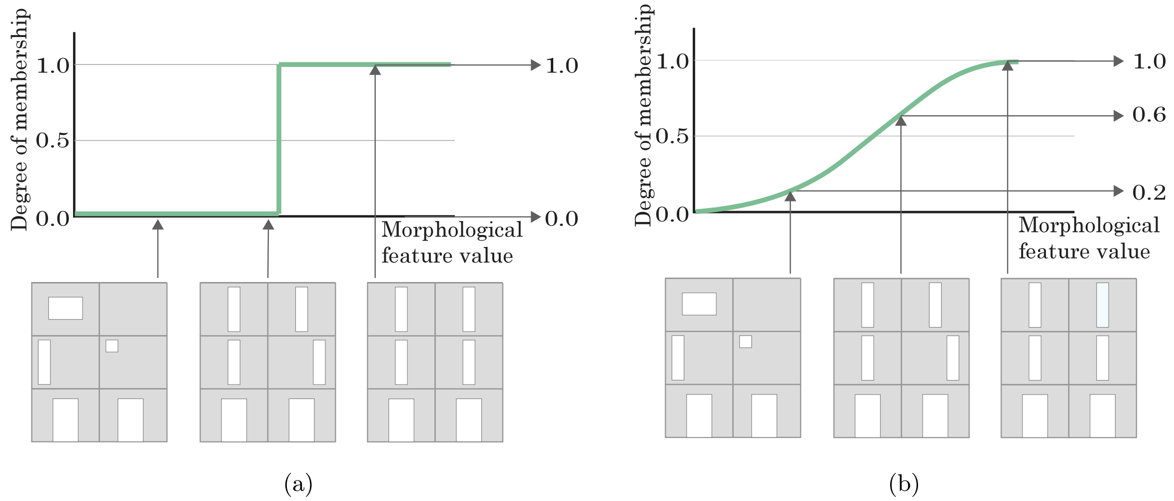

(a)

(b)

Fig. 2. Comparison between (a) sharp-edged and (b) continuous evaluation of a morphological feature (e.g., vertical symmetry of a building façade).

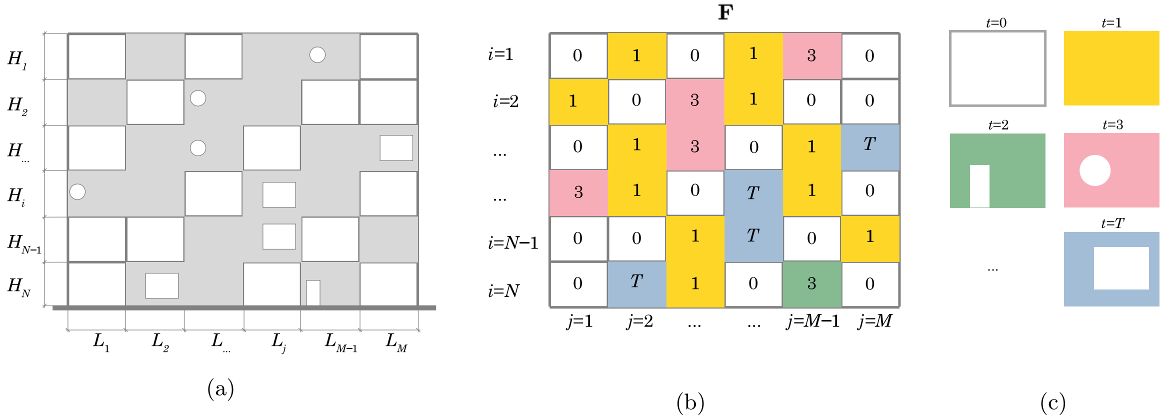

	j=1	j=2	…	…	j=M−1	j=M
i=1	0	1	0	1	3	0
i=2	1	0	3	1	0	0
…	0	1	3	0	1	*T*
…	3	1	0	*T*	1	0
i=N−1	0	0	1	*T*	0	1
i=N	0	*T*	1	0	3	0

(a)

(b)

(c)

Fig. 3. Schematic representation of the façade encoding: (a) façade with $N \times M$ fields; (b) block matrix **F** representing the façade divided into $N \times M$ blocks, each associated with a wall type identifier; (c) inventory of available wall types, including void field ($t_{i,j} = 0$), solid panel ($t_{i,j} = 1$) and various openings ($t_{i,j} = 2, \dots, T$).

Table 1
Summary of the proposed morphological metrics.

Metric	Symbol	Equation	Short description
Pattern	m_P	Eq. (A.3)	Evaluation of recurring sub-patterns in the façade.
Continuity	m_C	Eq. (A.6)	Assessment of the visual coherence by identifying the largest connected region in the façade.
Vertical symmetry	m_{S_V}	Eq. (A.7)	Quantification of the façade symmetry relative to the vertical axis (including possible flips).
Horizontal symmetry	m_{S_H}	Eq. (A.8)	Quantification of the façade symmetry relative to the horizontal axis (including possible flips).
Balance	m_B	Eq. (A.11)	Analysis of the distribution of filled areas between the left and right halves of the façade.
Rhythm	m_R	Eq. (A.14)	Examination of the periodic repetition of façade elements across storeys or bays.
Uniformity	m_U	Eq. (A.18)	Rating the even distribution of wall types across all storeys and bays of the façade.
Density	m_D	Eq. (A.19)	Rating the overall opacity of the façade.
Ground floor density	m_G	Eq. (A.20)	Appraisal of the transparency level of the façade at the ground floor only.
Edge density	m_E	Eq. (A.21)	Appraisal of the transparency level of the façade at the lateral edges only.

3.4. Fuzzy inference system for façade morphology assessment

Since ambiguity and perceptual variability are inherent in assessing façade appearance, designers may interpret the same morphological feature in different ways. For instance, in a conventional binary approach, a façade might be described as either ‘solid’ or ‘transparent’. Fuzzy sets provide a more nuanced framework, allowing the façade to be characterized more realistically as ‘solid’, ‘semi-transparent’, and ‘transparent’, each to a certain degree. In fuzzy logic, morphological features are therefore expressed through linguistic categories that capture these gradual transitions. Rather than forcing a metric value into exactly one category, it can belong to several categories at once, each to a certain degree of membership between 0 (meaning it does not fit the category) and 1 (meaning it fits perfectly) [47–49]. These degrees are determined by simple curves, known as membership functions, which map a numerical feature value to how well it corresponds to each descriptive label.

As an example, consider the ground-floor density metric evaluated through three categories as in Fig. 5. An input value of $m_G = 0.33$ has degree 0.30 in the ‘low’ category, a stronger degree 0.81 in ‘medium’ category, and 0.00 in ‘high’ category. In plain terms, this means that the ground floor is mostly semi-transparent, while exhibiting a relatively low solid appearance, but clearly not a high degree of density.

This operation exemplifies the fuzzification stage, in which numerical inputs are translated into linguistic categories through their associated membership functions. Several input–fuzzification strategies

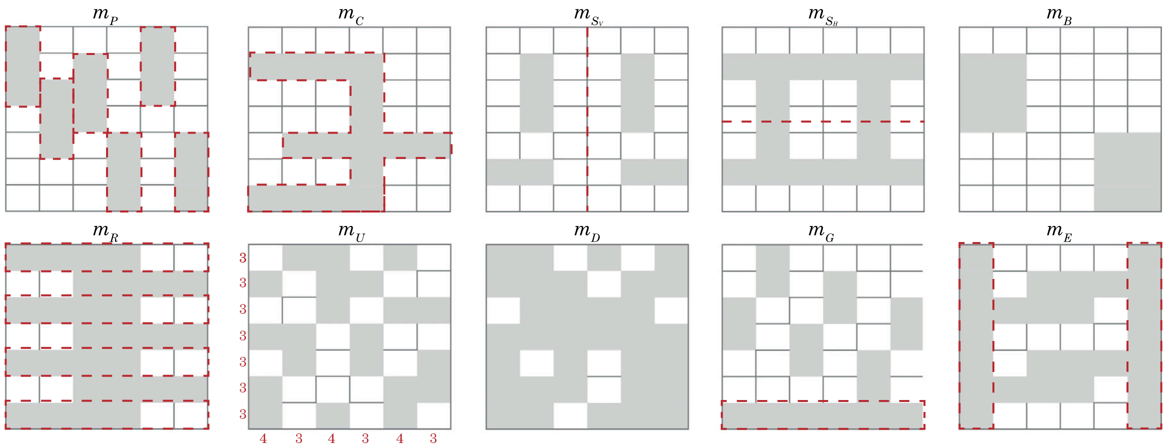

Fig. 4. Illustrative façade layouts ($N \times M = 7 \times 6$, solid panels only) achieving high values for each morphological metric listed in Table 1. Red annotations and dashed lines indicate the elements involved in the computation of selected metrics.

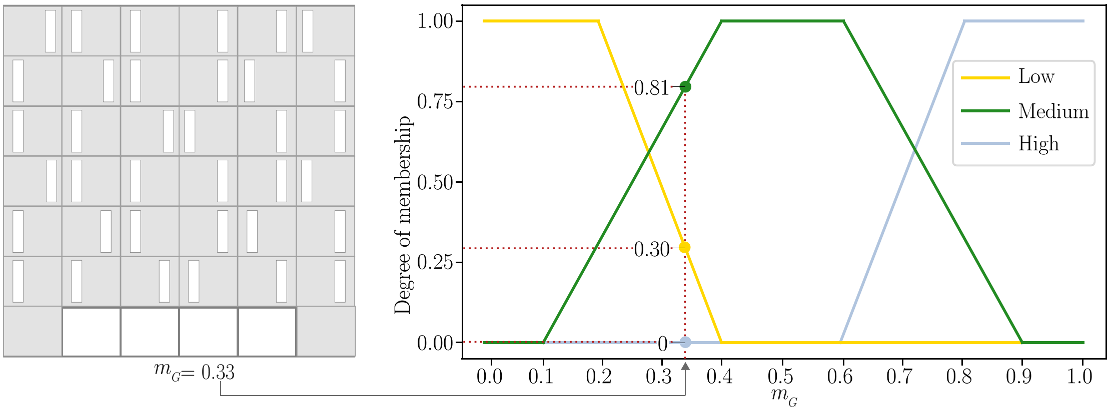

Fig. 5. Fuzzification of a morphological feature (e.g., ground floor density of a building façade).

have been proposed in the literature [e.g., 50,51], and although originally developed in other domains, these strategies can be adapted to the assessment of building façade morphology.

To ground the fuzzification stage in a formal framework, we introduce the mathematical definition of a fuzzy set. Let Ω_m denote the universe of discourse for a morphological variable. A fuzzy set $\mathcal{M} \subseteq \Omega_m$ is defined as the collection of ordered pairs [52]:

$$\mathcal{M} = \left\{ \left(m, \mu_{\mathcal{M}}(m) \right) \mid m \in \Omega_m \right\}, \tag{1}$$

where $\mu_{\mathcal{M}}(m)$ is the membership function (MF) of m in $\mathcal{M}$, taking values in the interval $[0, 1]$. A value of $\mu_{\mathcal{M}}(m)$ close to 1 indicates a high degree of membership of m in $\mathcal{M}$, whereas values near 0 correspond to non-membership. In other words, $\mu_{\mathcal{M}}(m)$ in Eq. (1) quantifies the extent to which the numerical feature m belongs to the linguistic category represented by $\mathcal{M}$. A FIS builds upon these fuzzified inputs by using a collection of fuzzy rules to map them to an output [53]. In general terms, each rule links a set of linguistic conditions on the input variables to a linguistic conclusion. A rule p takes the standard `IF–THEN` form [48]:

$$\texttt{Rule}\, p: \ \texttt{IF} \left\langle \mathit{antecedent}_p \right\rangle \texttt{THEN} \left\langle \mathit{consequent}_p \right\rangle, \tag{2}$$

where $\left\langle \mathit{antecedent}_p \right\rangle$ specifies the fuzzy conditions on one or more input variables, and $\left\langle \mathit{consequent}_p \right\rangle$ provides the resulting fuzzy output. A rule may involve multiple linguistic statements in both its antecedent and consequent. In the present framework, these rules are central because they encode the design intentions behind façade assessment: they determine how different morphological attributes interact and how their combined fuzzy evaluations produce an overall assessment.

Different types of FIS can then be constructed depending on how the consequents of the rules are formulated. Two main approaches are commonly used: the Mamdani method [54], in which the output is expressed as a fuzzy set, and the Takagi–Sugeno–Kang (TSK) method [55], in which the output is a mathematical function of the input variables (typically a constant or a linear expression). Mamdani's approach is preferred here, as it is suitable for dealing with human-centric and interpretation-based decision-making applications, while the Takagi–Sugeno–Kang's method is more common for control problems [53].

The problem of mapping from multiple input fuzzy sets to a single fuzzy output through the pth fuzzy rule in Eq. (2) (so-called multi-input–single-output Mamdani fuzzy rule) can be rewritten in the following general form [56]:

$$\begin{aligned} &\texttt{Rule}\, p: \ \texttt{IF}\, m_1 \in \mathcal{M}_{p1}\ \texttt{AND/OR/NOT}\ m_2 \in \mathcal{M}_{p2}\ \texttt{AND/OR/NOT} \ldots \texttt{AND/OR/} \\ &\quad \texttt{NOT}\, m_q \in \mathcal{M}_{pq}\ \texttt{THEN}\, n_p \in \mathcal{N}_p, \end{aligned} \tag{3}$$

where $m_1, m_2, \ldots, m_q$ are the inputs, $\mathcal{M}_{p1}, \mathcal{M}_{p2}, \ldots, \mathcal{M}_{pq}$ are the fuzzy sets representing the conditions for each input, n_p is the output of the pth fuzzy rule, and $\mathcal{N}_p$ denotes the fuzzy set representing the pth output. Moreover, common fuzzy logic operators have been introduced, namely `AND` (intersection), `OR` (union), and `NOT` (complement).

For two fuzzy sets $\mathcal{M}_g$ and $\mathcal{M}_\ell$, the logical `AND` (or intersection operator $\cap$) in Eq. (3) is defined such that [52,57]:

$$\begin{gathered} \mu_{\mathcal{M}_g \cap \mathcal{M}_\ell}(m_g, m_\ell) = \mu_{\mathcal{M}_g}(m_g)\, \mathrm{t}\, \mu_{\mathcal{M}_\ell}(m_\ell) \leq \min \left(\mu_{\mathcal{M}_g}(m_g), \mu_{\mathcal{M}_\ell}(m_\ell) \right) \\ \forall m_g \in \Omega_{m_g}, \forall m_\ell \in \Omega_{m_\ell}, \end{gathered} \tag{4}$$

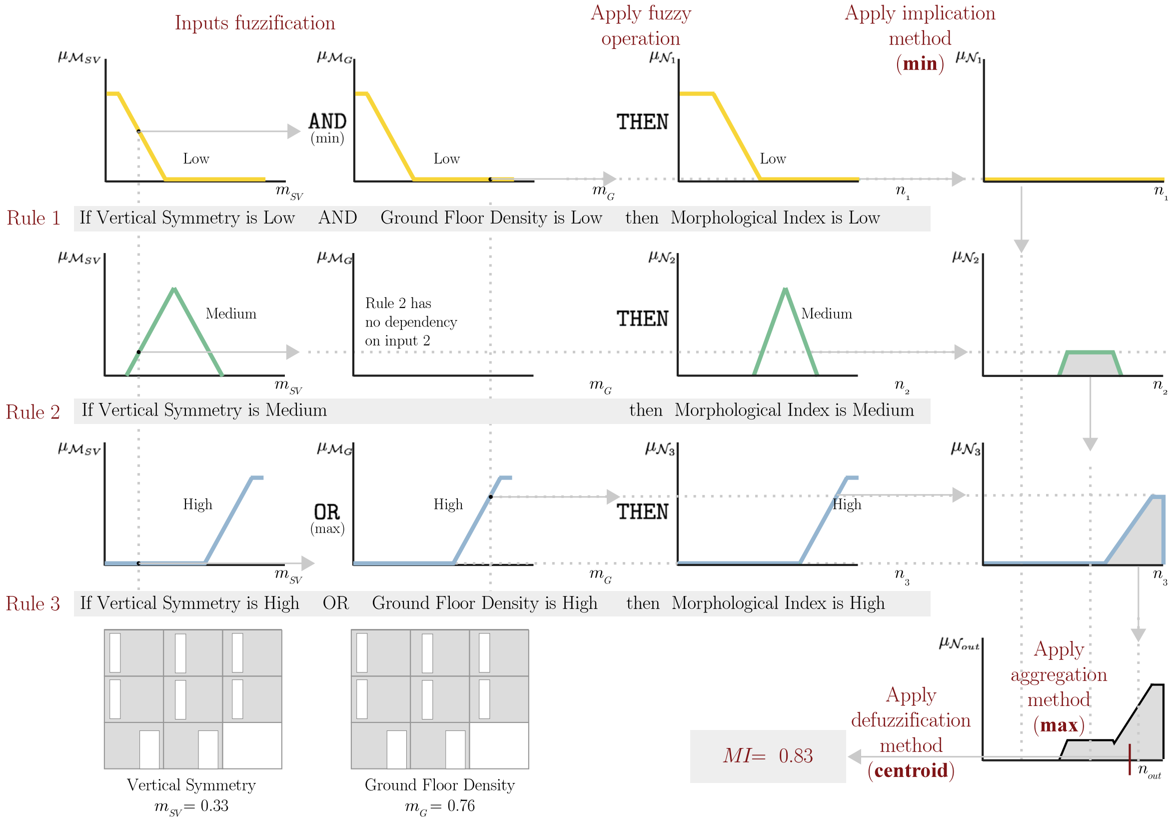

Fig. 6. Illustration of a Mamdani-type FIS applied to calculate the MI.

where t is the t- or triangular norm. The logical `OR` (or union operator ∪) in Eq. (3) is instead defined such that [52,57]:

$$\mu_{\mathcal{M}_g \cup \mathcal{M}_\ell}(m_g, m_\ell) = \mu_{\mathcal{M}_g}(m_g)\,\mathrm{s}\,\mu_{\mathcal{M}_\ell}(m_\ell) \leq \max\left(\mu_{\mathcal{M}_g}(m_m), \mu_{\mathcal{M}_\ell}(m_\ell)\right)$$
$$\forall m_g \in \Omega_{m_g}, \forall m_\ell \in \Omega_{m_\ell}, \tag{5}$$

where s is the s- or triangular co-norm. Both t-norm and s-norm are non-decreasing (monotonically) in each argument; they are commutative, associative, and satisfy boundary conditions. The most common t-norms are the intersection and the algebraic product, while the most common s-norms are the union and algebraic sum. The relation between s- and t-norms is given by the equivalent of the De Morgan's laws in set theory. In Eq. (3), the logical `NOT` operator (corresponding to the complement) of a fuzzy set $\mathcal{M}_\ell$ is defined such that [52,57]:

$$\mu_{\bar{\mathcal{M}}_\ell}(m_\ell) = 1 - \mu_{\mathcal{M}_\ell}(m_\ell) \text{ for } \forall m_\ell \in \Omega_{m_\ell}. \tag{6}$$

Fuzzy logic operators can be implemented depending on the project targets and/or the designer's preferences.

The outputs of all pth fuzzy rules derived from Eq. (3) are then combined to obtain a single fuzzy output set $\mathcal{N}_{out} = \left\{ \left(n_{out}, \mu_{\mathcal{N}_{out}}\left(n_{out}\right) \right) \mid n_{out} \in \Omega_{n_{out}} \right\}$. This aggregation is accomplished by using the fuzzy logic operator `OR`. After fuzzy conclusions are combined, the so-called defuzzification step is performed [58]. The center-of-area method is used for defuzzification, taking the output as the balance point of the aggregated membership function, which provides a crisp value known as the centroid [58,59]. This step transforms the fuzzy output distribution into a crisp value that represents the final result of the FIS, which is the MI value.

Fig. 6 illustrates the general workflow of the Mamdani approach applied to the computation of the MI, using vertical symmetry and ground floor density as input features.

Each numerical input is first mapped into linguistic categories (e.g., 'low', 'medium', 'high') through the fuzzification stage. The fuzzy rules then evaluate these linguistic inputs through logical operators such as `AND` or `OR`, resulting in an activation degree for each rule. Through the Mamdani implication method, this activation degree is applied to the corresponding consequent fuzzy set, typically by truncating its membership function. Consequent sets are described using membership functions defined independently of the input membership functions. These sets reflect the semantics of the consequent and may differ in scale or shape from the input domains, as shown in Fig. 6. In the first rule, one of the input memberships is zero, and the `AND` operator therefore yields a zero activation degree. Under the Mamdani implication method, the consequent fuzzy set is truncated at this activation level, which collapses it to the zero membership function. This is why the resulting output of Rule 1 appears as a flat line along the horizontal axis in the figure. Rule 2's antecedent includes only a condition on the first input variable, in contrast to Rule 1. This indicates that the only factor influencing Rule 2's activation is Input 1's degree of membership in the relevant linguistic category. The strength of this rule is unaffected by Input 2 since it is excluded from the antecedent. In fact, using rules that rely on different subsets of inputs is a typical way to represent context-sensitive relationships in fuzzy models. Finally, Rule 3 has a nonzero activation degree, so its consequent fuzzy set is only partially truncated, preserving its shape and contributing to the final aggregated output. After all rule consequents are computed, they are aggregated using the fuzzy `OR` (maximum) operator. The crisp output shown in Fig. 6 ($MI = 0.83$, in this example) corresponds to the centroid of the aggregated fuzzy distribution. More precisely, the value 0.83 is the abscissa of the center-of-area of the combined output sets after applying the contributions of the rules. The pseudocode for this FIS, outlining the steps from input fuzzification to output defuzzification, is provided in the Supplementary Material (Algorithm S1).

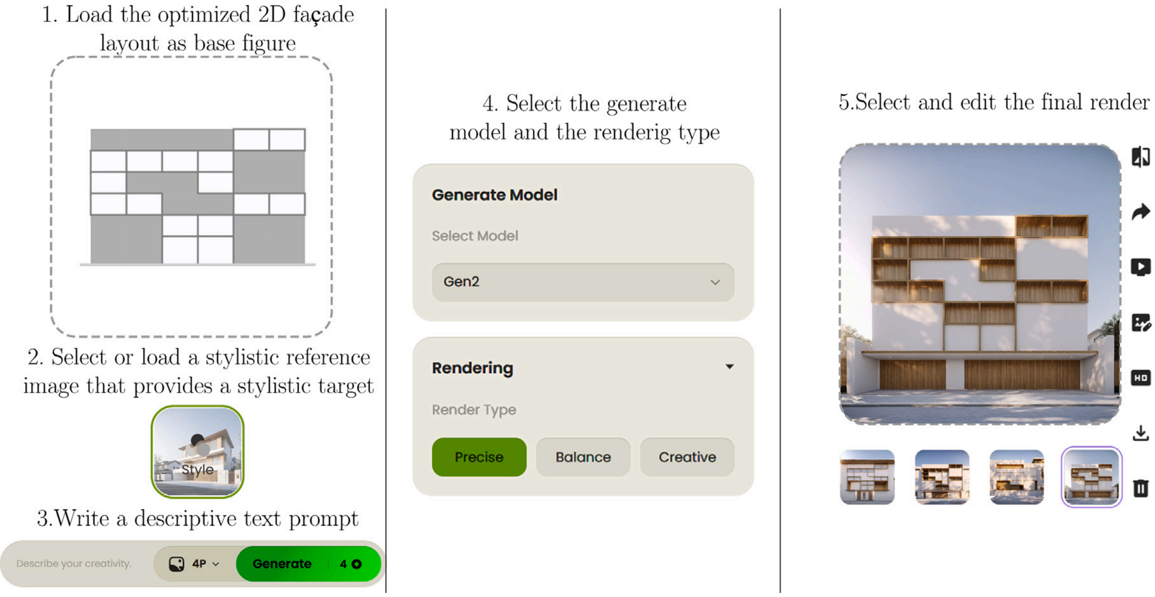

Generate Model
Select Model: Gen2

Rendering
Render Type: Precise | Balance | Creative

Fig. 7. Illustration of AI-powered conceptual visualization.

3.5. Morphology-based optimal design of the façade

The output of the FIS provides a crisp value that reflects the façade morphology according to designers' preferences. Hence, it can be employed to incorporate the morphology into the automated optimal design of the façade, potentially alongside other relevant — and possibly conflicting — objectives. To achieve this, the design problem involves selecting wall types from the user-defined wall inventory for each field of the façade. Under the assumption that the heights H_i and lengths L_j of each field in the façade are a priori constant values $\forall i, j$, let $\mathbf{x} = \begin{bmatrix} t_{1,1} & \dots & t_{i,j} & \dots & t_{N,M} \end{bmatrix}$ denote the design vector that collects the type of wall assigned to each field. By converting the MOO problem into a single-objective one using the weighted sum approach [60–62], the façade design can be generally formalized as follows:

$$\min_{\mathbf{x}} \left(\sum_r \omega_r f_{obj,r}(\mathbf{x}) \right) \qquad (7)$$

$$\mathbf{x} \in \mathcal{T}^{N \times M},$$

where $f_{obj,r}$ is the rth objective function referring to a specific design goal (such as morphology, energy efficiency, cost, environmental impact, thermal comfort, acoustic comfort, and structural performance), while ω_r is a factor introduced to weight their relative importance. The condition in Eq. (7) aims at obtaining an optimal layout of the façade by selecting the panel type from the assigned inventory $\mathcal{T}$. As a consequence, Eq. (7) represents a discrete optimization problem, with $\mathcal{T}^{N\times M}$ denoting the Cartesian product of $\mathcal{T}$ with itself $(N \times M)$ times, which defines the discrete $(N \times M)$-dimensional search space where each component of $\mathbf{x}$ is an element of the inventory $\mathcal{T}$.

3.6. AI-powered visualization

The final step of the proposed framework is dedicated to translating the abstract, optimized layouts into tangible visualizations. This step aims to show that solutions generated as a result of an optimization procedure can form the basis for compelling design concepts. The process employs a generative AI model capable of performing a multimodal translation, guided by several key inputs and parameters set by the designer. These include three primary inputs (see Fig. 7): (1) the optimized 2D façade layout, which defines the fundamental arrangement of solid and void elements; (2) a stylistic reference image that provides a stylistic target; and (3) a descriptive text prompt to specify materials, atmosphere, and context.

In addition to these inputs, the designer sets a crucial control parameter, the render type, which modulates the model's interpretive freedom. This setting offers modes such as 'precise', 'balance', or 'creative'. A 'precise' setting instructs the model to adhere strictly to the inputs, while a 'creative' setting allows for greater artistic license and deviation. The 'balance' mode provides a trade-off between fidelity and innovation. The underlying technology, as exemplified by platforms like the LookX AI Cloud platform [63], uses these combined directives to condition advanced generative models. The model synthesizes a high-fidelity rendering that is immediately intelligible to designers and stakeholders, thereby facilitating the effective connection of computational logic with creative representation and informing subsequent design decisions, in a process where human input remains essential also for final judgment and design selection.

4. Numerical investigations setup

This section describes the numerical setup adopted to apply the proposed framework in a series of design scenarios. It specifies the configuration of the fuzzy inference system and the optimization strategy (Section 4.1), defines the wall inventory and design data (Section 4.2), and outlines the set of test cases used to explore the behavior of the method under increasing levels of complexity (Section 4.3).

4.1. Inference engine configuration and optimization strategy

For the following numerical applications, the FIS was configured using the `scikit-fuzzy` library [64]. The MFs for the antecedents and the consequent (i.e., the MI) are shown in Fig. 8. Decreasing and increasing stepwise linear functions were used for the 'low' and 'high' sets, while a triangular function was employed for the 'medium' set. The fuzzy operators involved in the rules of the FIS were the minimum t-norm for the `AND` conjunction and the maximum s-norm for the `OR` disjunction.

Regarding the optimization problem, in the following applications, the general MOO formulation in Eq. (7) is limited to a single-objective problem to focus on maximizing the MI. Accordingly, the design problem takes the following form:

$$\max_{\mathbf{x}} \left(MI(\mathbf{x}) \right). \qquad (8)$$

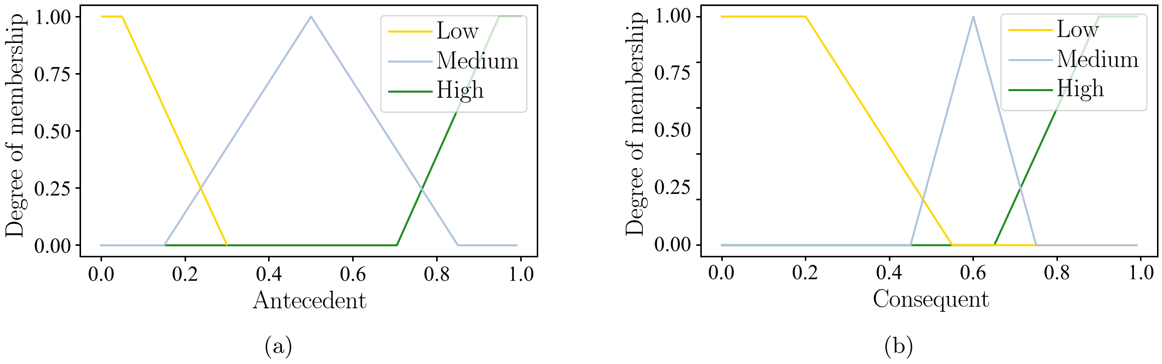

Fig. 8. Configuration of the FIS: MFs for (a) all input variables (antecedents) and (b) the output variable, namely the MI (consequent).

The optimization problem defined in Eq. (8) involves a discrete search space and is solved using a GA. The pseudocode for this GA is provided in the Supplementary Material (Algorithm S2). It is implemented using the `pymoo` framework [65] and configured with specific settings (e.g., a 4-point crossover operator with probability $p_c = 0.4$ [66] and a polynomial mutation with probability $p_m = 0.5$ and parameter $\eta = 3$ [67,68]) that were selected for their efficiency and speed in solving a test optimization scenario. For an assessment of the algorithm's sensitivity to these and other parameters, including their impact on computational time and convergence, refer to the Supplementary Material (Table S1). Since the design variables — representing wall types — are integers, they are managed within the real-valued GA using a rounding repair mechanism to ensure feasibility [69].

The initial population size was scaled in proportion to the number of design variables and the complexity of the scenario. For instance, for a baseline 6 × 6 façade, a population of 1440 individuals (40 times the length of the design vector) was used. A hybrid initialization strategy is employed to balance exploration and exploitation from the outset [70–72]. Specifically, 40% of the initial population is generated using latin hypercube sampling and refined with 100 local search iterations. The remaining 60% is generated using a Sobol sequence, seeded from the refined individuals. This approach is designed to create a diverse initial population that is also biased toward high-performance regions of the search space, accelerating convergence.

At the end, the environmental performance of the façade is assessed as a secondary outcome. This allows for the evaluation and ranking of the top-performing solutions that emerge from the morphology-driven optimization. The environmental impact is quantified by the raw embodied carbon dioxide equivalent, $E_{raw}(\mathbf{x})$:

$$E_{raw}(\mathbf{x}) = \sum_{i=1}^{N} \sum_{j=1}^{M} A_{i,j} e_{i,j}(\mathbf{x}) \tag{9}$$

where $A_{i,j} = H_i \cdot L_j$ is the area of the (i,j)th field and $e_{i,j}(\mathbf{x})$ is the embodied carbon dioxide equivalent of the wall in the (i,j)th field.

4.2. Set of wall types

Fig. 9 illustrates the complete wall inventory $\mathcal{T}$ considered in the following numerical investigations. It is important to note that this specific inventory is illustrative; the framework's design allows for the definition of any custom wall types and associated properties by the user. The inventory explores a range of morphological features, beginning with basic states — an empty field and a solid panel — and progressing to more complex arrangements. These configurations include variations in window placement (e.g., centered, corner, shifted), quantity (single, double), and aspect ratio (square, tall, long), as well as a central door. A key aspect is the treatment of the symmetry condition. As detailed in Table 2, this is determined not only by the own symmetry of the wall but also by its relationship to the counterpart generated via pre-defined flipping functions, namely $\mathrm{flip_H}(t)$ and $\mathrm{flip_V}(t)$. These functions map a given wall type t to its horizontally or vertically reflected pair within the inventory, allowing the symmetry metrics (Eqs. (A.7) and (A.8)) to evaluate matched asymmetric elements. For instance, the left-shifted window ($t = 3$) is the vertical counterpart of the right-shifted window ($t = 4$), such that $\mathrm{flip_V}(t = 3) = 4$.

To assess the environmental performance of the façade as in Eq. (9), embodied carbon dioxide equivalent values are also listed in Table 2 and are determined based on the Environmental Product Declaration (EPD). The calculations consider life-cycle stages A1–A3 (covering raw material supply through manufacturing) and D (benefits and loads beyond the system boundary). For the solid panels, Rubner-XLAM [73] Cross-Laminated Timber (CLT) is selected. Based on its EPD from the IBU platform [74], the resulting embodied carbon dioxide equivalent value, converted to a per-square-meter basis for a 9-cm thick panel, is $e_{CLT} = -93.0\ \mathrm{kgCO_2e/m^2}$. This negative value is significant, as it reflects the biogenic carbon sequestered during the wood's growth. For glazed elements, the extreme-aluminum top double-glazing variant (F3) [75] is used. This module yields an embodied carbon equivalent value of $e_{glass} = 96.99\ \mathrm{kgCO_2e/m^2}$ per functional unit (defined as 1 $\mathrm{m^2}$ over a 30-year service life).

4.3. Design data and scenarios

To demonstrate the effectiveness and versatility of the proposed framework, seven Design Scenarios are analyzed. Through this set of applications, the feasibility and adaptability of the proposed approach are systematically demonstrated. These scenarios feature progressively increasing complexity to test the framework's performance under diverse morphological requirements. As detailed in Table 3, the scenarios vary in key parameters, including façade dimensions, the customizable inventory of available wall types, and designers' fuzzy rule sets embodying architectural intent, thereby providing a comprehensive assessment of the methodology across a range of design challenges.

By considering relatively simple building façade geometries and a limited set of morphological requirements, case studies from DS0 to DS4 enable the assessment of the overall validity of the automated optimization process guided by the proposed MI under controlled conditions. The initial scenarios, DS0 and DS1, establish a baseline with 36 design variables (on a 6 × 6 grid) and a minimal inventory of just two wall types ($t \in [0, 1]$), creating a search space of 2^{36} possible façades. Subsequent scenarios, DS2 and DS3, vary the façade dimensions (up to a 5 × 8 grid) while progressively expanding the wall inventory to three and then five types, respectively. The complexity culminates in DS4, which, despite returning to a 6 × 6 grid, utilizes the full inventory of 12 wall types. This dramatically increases the discrete search space to 12^{36} configurations, creating a more challenging optimization defined by numerous competing morphological requirements. Finally, DS5 acts as a controlled study to demonstrate stylistic differentiation using larger grid sizes. This scenario models a pair of 'twin towers' with 125 variables (5 × 25 grid for DS5a) and 100 variables (5 × 20 grid for

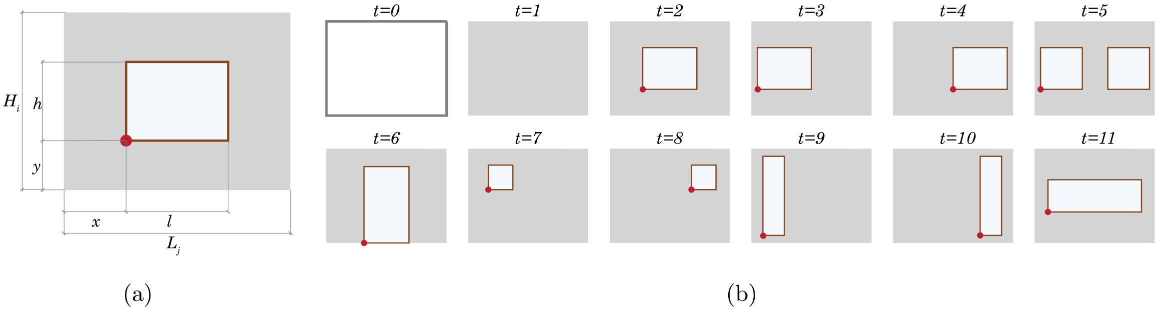

Fig. 9. Wall inventory: (a) general wall layout with opening geometry; (b) proposed wall types ($t = 0$–11) illustrating variations in window and door configurations (red dot indicates the window origin).

Table 2
Wall inventory: wall types (t), symmetry mappings (flip_H, flip_V), window dimensions (l, h), window origin coordinates (x, y), and associated embodied carbon values.

t	Description	$\mathrm{flip}_H(t)$	$\mathrm{flip}_V(t)$	Window size		Window origin		e_{glass}	e_{CLT}
				l [cm]	h [cm]	x [cm]	y [cm]	[kgCO$_2$e]	[kgCO$_2$e/m^2]
0	Empty field	$t = 0$	$t = 0$	N/A		N/A		N/A	0
1	Full field	$t = 1$	$t = 1$	N/A		N/A		N/A	
2	Square window in the middle	$t = 2$	$t = 2$	140	120	$L_j - (l/2)$	100	162.9	
3	Square window on the left	$t = 4$	$t = 3$	140	120	20	100	162.9	
4	Square window on the right	$t = 3$	$t = 4$	140	120	$L_j - (l + 20)$	100	162.9	
5	Two square windows	$t = 5$	$t = 5$	120	120	20	100	139.6	
6	Door in the middle	$t = 6$	N/A	90	215	$L_j - (l/2)$	0	187.7	−93.0
7	Small square window in the top-left corner	$t = 8$	N/A	60	60	20	100	34.9	
8	Small square window in the top-right corner	$t = 7$	N/A	60	60	$L_j - (l + 20)$	100	34.9	
9	Tall thin rectangular window on the left	$t = 10$	$t = 9$	60	140	20	$H_i - (h/2)$	81.5	
10	Tall thin rectangular window on the right	$t = 9$	$t = 10$	60	140	$L_j - (l + 20)$	$H_i - (h/2)$	81.5	
11	Long horizontal rectangular window	$t = 11$	$t = 11$	140	60	$L_j - (l/2)$	100	81.5	

Table 3
Design scenarios for different building façades together with assigned geometric data, wall types, and design rules.

Design scenario	$N \times M$	H L	$t_{i,j}$	Rules
DS0	6 × 6	$H = 1_6 \times 3.0$ m $L = 1_6 \times 6.0$ m	$t_{i,j} \in [0, 1]$	Pattern (high) Continuity (low)
DS1	6 × 6	$H = 1_6 \times 3.0$ m $L = [3.0, 6.0, 6.0, 6.0, 6.0, 3.0]$ m	$t_{i,j} \in [0, 1]$	Vertical symmetry (high) Pattern (high) Continuity (low OR medium)
DS2	5 × 8	$H = 1_5 \times 3.0$ m $L = [6.0, 6.0, 3.0, 6.0, 6.0, 3.0, 6.0, 6.0]$ m	$t_{i,j} \in [0, 1, 2]$	Rhythm (high) Balance (high) Density (medium)
DS3	7 × 5	$H = 1_7 \times 4.0$ m $L = 1_5 \times 5.0$ m	$t_{i,j} \in [0, 1, \dots, 4]$	Horizontal symmetry (high) Uniformity (high) Ground floor density (low OR medium)
DS4	6 × 6	$H = 1_6 \times 3.0$ m $L = [3.0, 3.0, 3.0, 6.0, 6.0, 6.0]$ m	$t_{i,j} \in [0, 1, \dots, 11]$	Density (medium OR high) Continuity (high) Ground floor density (low OR medium) Balance (low) Edge density (medium)
DS5a	5 × 25	$H = 1_{25} \times 3.0$ m $L = 1_5 \times 6.0$ m	$t_{i,j} \in [0, 1]$	Pattern (medium) Density (medium) Ground floor density (low) Continuity (medium OR high) Balance (high) Vertical symmetry (low OR medium) Edge density (medium)
DS5b	5 × 20	$H = 1_{20} \times 3.0$ m $L = 1_5 \times 6.0$ m	$t_{i,j} \in [0, 1]$	Pattern (high) Density (medium OR low) Ground floor density (low) Continuity (low) Balance (high) Vertical symmetry (high) Edge density (low)

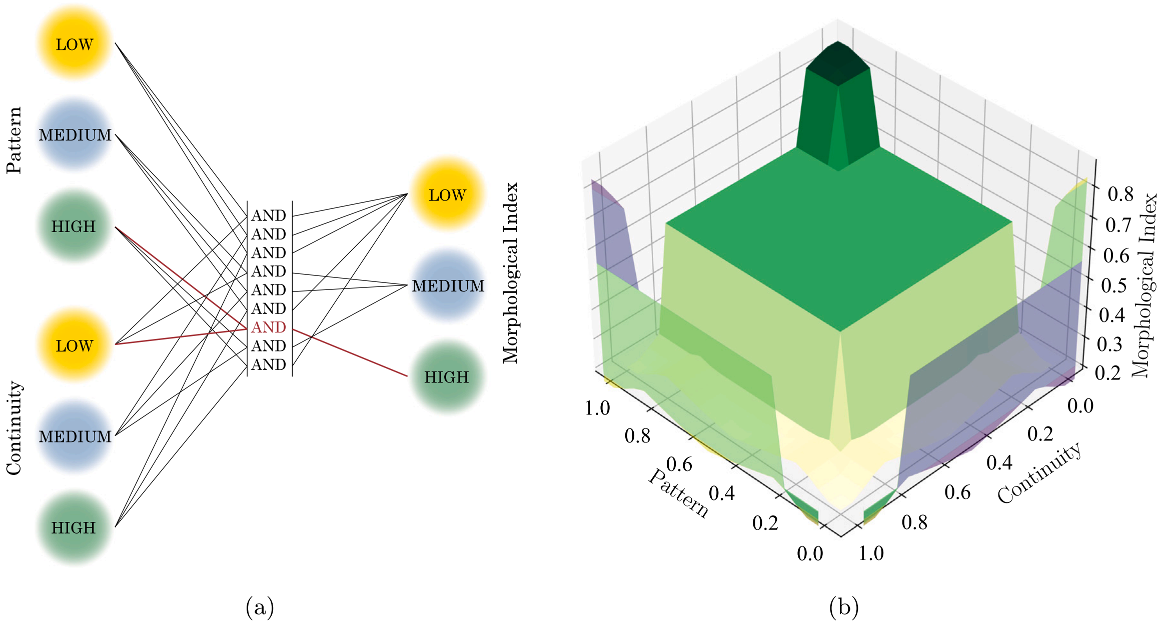

Fig. 10. Design scenario DS0: (a) fuzzy rules; (b) visualizations of the MI.

DS5b). Despite the larger scale, these scenarios revert to the simple two-type wall inventory to highlight the framework's capacity to produce unique architectural expressions – one emphasizing balanced massing and the other a lighter, more symmetrical appearance – only through the manipulation of the designer's preferences.

5. Results

This section reports the outcomes of the numerical investigations introduced in Section 4. For each design scenario (DS0–DS5), we present representative high-scoring façade layouts together with convergence behavior and the corresponding values of the MI and relevant morphological metrics. Environmental performance is reported as a secondary indicator to support comparison among solutions with similar morphological scores.

5.1. Pattern and continuity (DS0)

The first design scenario, DS0, serves as a baseline to evaluate the framework's core functionality in a controlled setting. This scenario uses a simple 6 × 6 grid with a minimal inventory of only two wall types ($t_{i,j} \in [0,1]$), representing solid and void panels. The main goal is to generate highly fragmented façades by applying fuzzy rules that reward high pattern and low continuity. The interaction between these two metrics, as defined by the fuzzy rules (Fig. 10(a)), is visualized in Fig. 10, which illustrates how the MI score changes based on the input metric values (Fig. 10(b)).

Fig. 11(a) shows that the population's fitness rapidly improves, with the best solutions stabilizing at a high MI value of approximately 0.93 by generation 25. The progression of the individual metrics for the best-found solution, plotted in Fig. 11(b), reflects the design rules: the pattern metric is maximized, reaching its theoretical optimum of 1.0, while the continuity metric is minimized, declining to a value of approximately 0.1. This progression is typical of the algorithm's convergence across all design scenarios, thus it is presented here for illustrative purposes only.

From a pool of 1440 individuals in the final generation, 307 (21.3%) achieved the maximum MI of 0.93, indicating robust convergence toward a specific morphological solution. This MI value of 0.93 was consistently achieved by the optimization procedure across multiple runs, denoting the global optimum for this scenario. However, the algorithm identified multiple distinct façade layouts that yielded the same optimal value of the objective function. The final optimized layouts, presented in Fig. 12, exhibit a distinct architectural character consistent with the targeted requirements. Within this large pool of optimal solutions, a recurrent configuration emerges, consisting of 14 solid panels, which corresponds to an embodied carbon value of −20.47 tonCO$_2$e. The optimized façades in Fig. 12 reflect the strategic resolution of the two competing morphological requirements. To illustrate the variation in environmental impact, here and henceforth the optimal layouts were grouped into four CO$_2$ emission quantiles, with four random layouts sampled from each group. Each row in the figure corresponds to one quantile, arranged from most environmentally favorable (top) to least favorable (bottom). The requirement for a high pattern score was met by establishing and repeating a minimal sub-pattern — typically an arrangement of solid panels spanning two adjacent bays. This modular unit was then shifted horizontally between storeys, a strategy that effectively breaks up vertical and horizontal alignments, thus satisfying the requirement for low continuity. While the solutions in Fig. 12 achieve the same MI, they exhibit significant variation in environmental performance (sequestered tonCO$_2$e), providing the designer with a set of high-performing layouts for a final, informed selection.

5.2. Vertical symmetry, pattern, and continuity (DS1)

The second design scenario, DS1, investigates the impact of adding a strong geometric constraint to the baseline problem. While retaining the same 6 × 6 grid and the minimal two-type wall inventory of DS0, the fuzzy rules set is updated to require high vertical symmetry in addition to high pattern while the continuity requirement is slightly relaxed to allow for low-to-medium values. This scenario is designed to test how the optimization process navigates the interplay between the existing and new morphological requirements.

It is evident that the morphological outcome is altered when vertical symmetry is included, leading to a different set of optimized solutions as shown in Fig. 13. The convergence toward the optimal solution is notably tighter in this case: out of 1800 individuals in the final generation, only 59 (3.3%) achieved the maximum MI of 0.87. The top-performing layouts for DS1 are all now characterized by a strongly symmetrical organization. The optimization process satisfied this requirement through two primary strategies: either by forming centrally

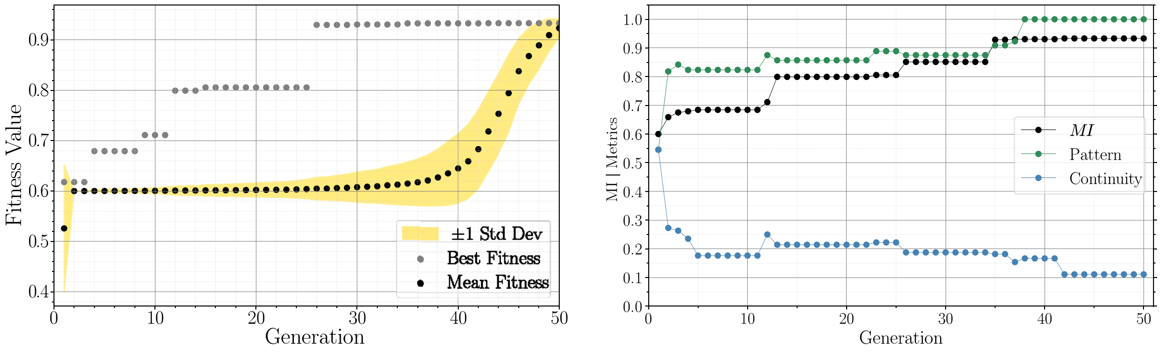

(a) (b)

Fig. 11. Optimization performance for design scenario DS0: (a) evolution of population fitness over 50 generations; (b) evolution of the MI and its contributing metrics for the best individual in each generation.

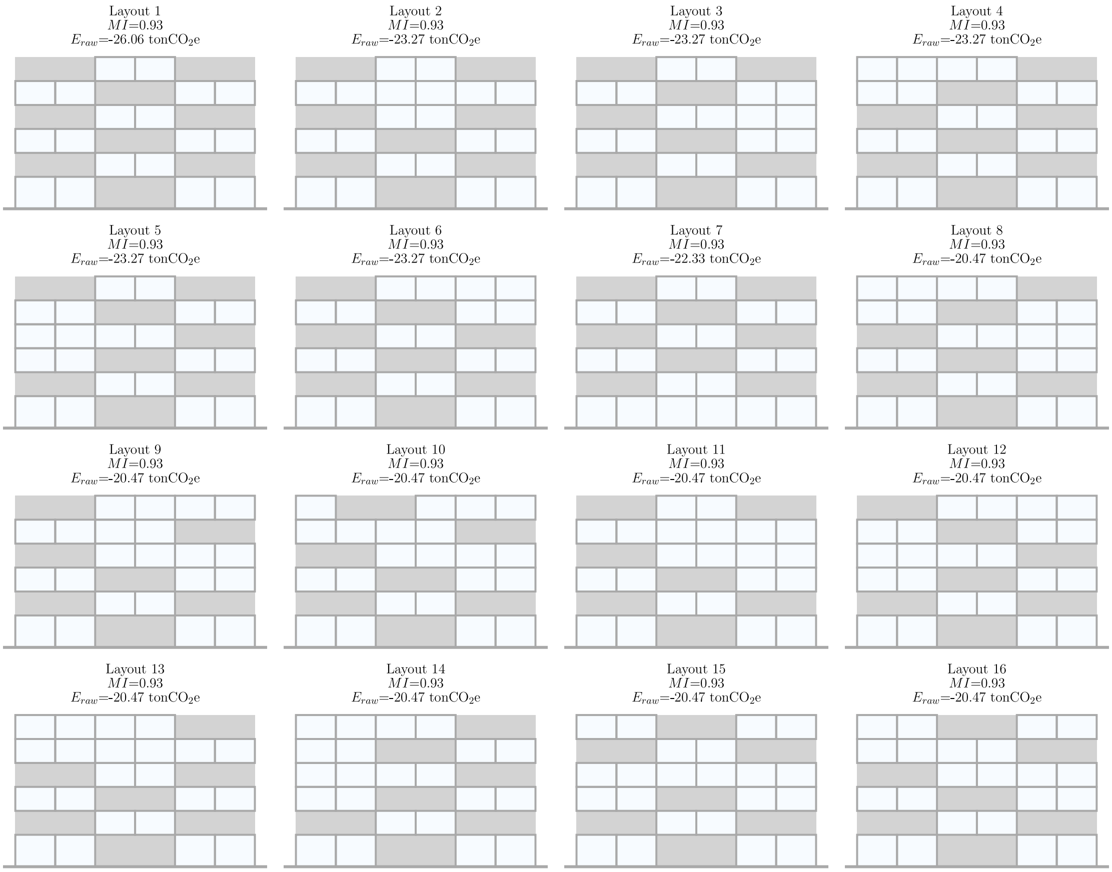

Fig. 12. Top-performing façade layouts for design scenario DS0.

aligned (solid or empty) strips that span multiple bays or by mirroring the minimal two-bay modular unit across the façade's central axis. The requirement for low-to-medium continuity is primarily fulfilled by introducing horizontal breaks, using empty storeys to interrupt otherwise continuous vertical strips. Since enforcing vertical symmetry requires more solid panels to achieve balanced compositions, a larger potential for sequestered carbon dioxide compared to the sparser, non-symmetric solutions from DS0 is obtained.

5.3. Rhythm, balance, and density (DS2)

Design Scenario DS2 advances the complexity. The problem is defined on a larger 5 × 8 grid with alternating bay widths, a geometric setup that discourages simple symmetry. The wall inventory is expanded to include a centered window unit ($t_{i,j} \in [0, 1, 2]$), allowing for greater variation in transparency. The fuzzy rules for this scenario target a sophisticated expression by requiring high rhythm, high balance, and medium density.

The optimization results, shown in Fig. 14, reveal that the algorithm successfully navigated this highly constrained problem. The convergence is tight, with only 34 individuals of 1800 individuals (1.9%) achieving the maximum MI of 0.76, indicating a sparse distribution of optimal solutions within the vast search space. The analysis of these top-performing layouts reveals the specific strategies the GA discovered to meet the tripartite requirements. The requirement for high rhythm is consistently met through the formation of vertical bands, where

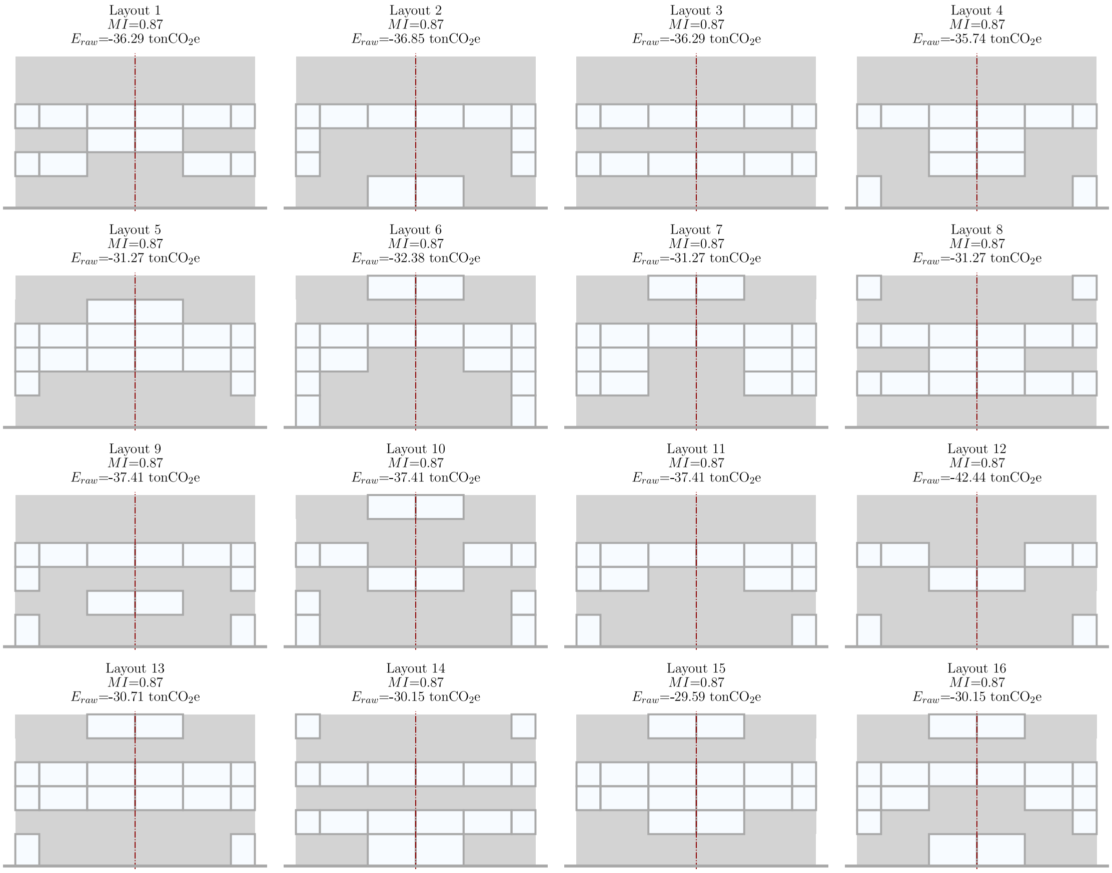

Fig. 13. Top-performing façade layouts for design scenario DS1.

Fig. 14. Top-performing façade layouts for design scenario DS2.

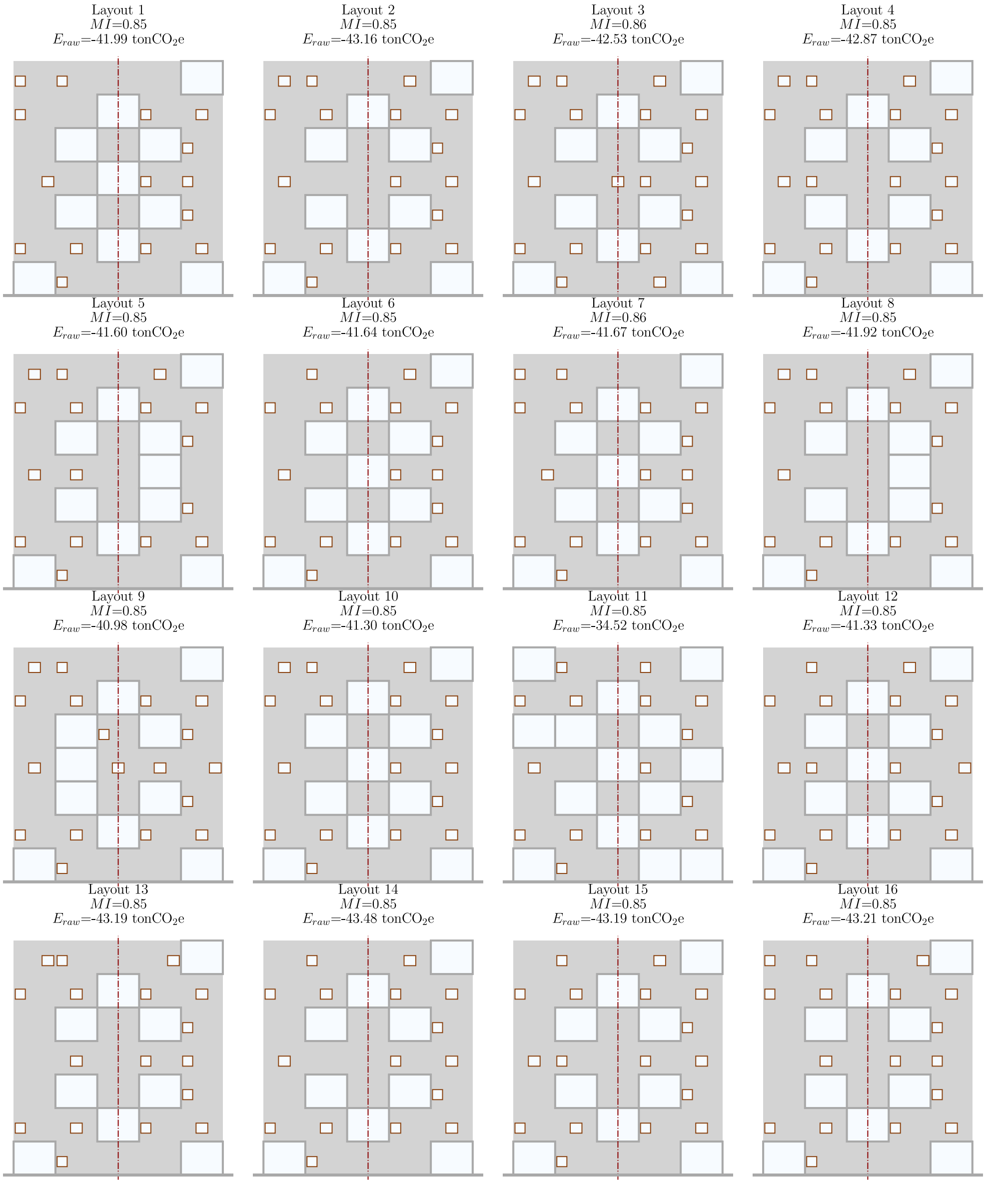

Fig. 15. Top-performing façade layouts for design scenario DS3.

columns of windowed panels create a strong visual pulse across the façade, a direct response to the irregular bay widths. The need for high balance is achieved through two distinct approaches. Some solutions, such as Layout 2, exhibit near-perfect symmetry. Others, like Layouts 1 and 4, achieve an asymmetric condition by carefully distributing infilled and void elements across the horizontal axis. At the same time, the medium density is satisfied by interspersing panels with the transparent window units, resulting in façades that are neither monolithic nor overly glazed.

5.4. Horizontal symmetry, uniformity, and ground floor density (DS3)

Design Scenario DS3 features a façade configured as a 7 × 5 grid with constant bay widths and variable storey heights. The complexity is further increased by expanding the wall inventory to five types ($t_{i,j} \in [0, \ldots, 4]$), which includes progressively more opaque panels. The fuzzy rules are designed to enforce a stable, orderly composition by requiring high horizontal symmetry and high uniformity, along with low-to-medium ground floor density.

The optimization results for DS3, presented in Fig. 15, reveal a robust convergence toward the desired architectural character. From the final generation of 5250 individuals, only 31 (0.6%) achieved the maximum MI of 0.85, indicating that the optimal solution lies in a highly specific and narrow region of a complex search space. The visual output confirms the success of the optimization. The layouts consistently exhibit strong, though not always perfect, horizontal symmetry, often with only a few panels deviating from a pure mirrored state. Similarly, the high uniformity is evident in the even distribution of elements across both storeys and bays. The final MI score remains below the theoretical maximum because of the inherent trade-offs: for instance, achieving perfect uniformity can conflict with achieving perfect horizontal symmetry.

5.5. Density, continuity, balance, ground floor density, and edge density (DS4)

Design Scenario DS4 represents the most complex challenge, designed to test the framework's ability to synthesize a wide range of competing constraints into a coherent architectural solution. It is defined on a 6 × 6 grid with varied bay widths and utilizes the full inventory of 12 wall types, creating a vast space. The fuzzy rules for

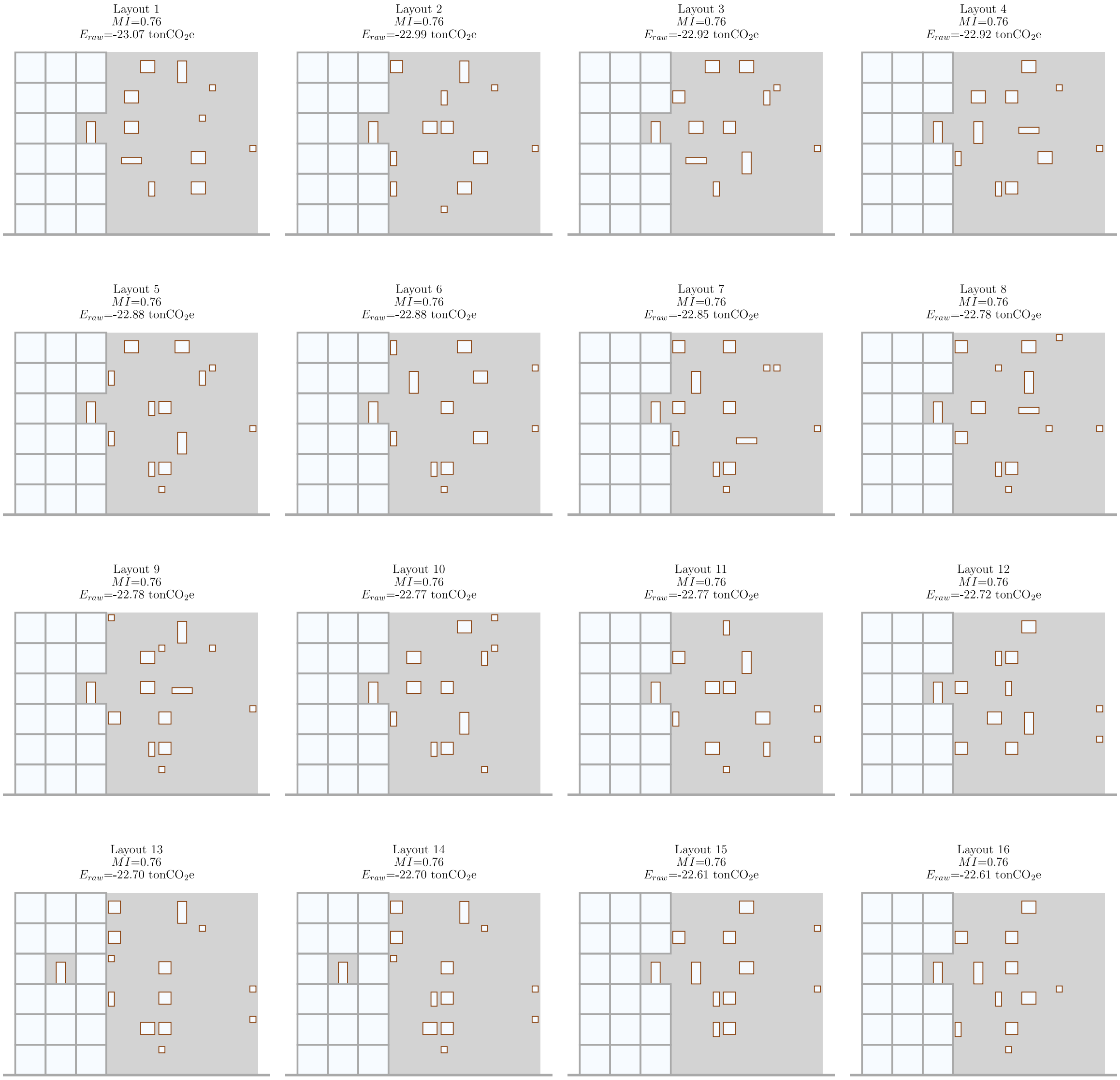

Fig. 16. Top-performing façade layouts for design scenario DS4.

this scenario intentionally omit any rules related to formal ordering principles like symmetry, rhythm, or pattern. Instead, it imposes a multifaceted set of five simultaneous requirements: medium-to-high density, high continuity, low balance, medium ground floor density, and medium edge density.

The optimization results, presented in Fig. 16, demonstrate a remarkable convergence towards a specific and unconventional architectural concept. Despite the problem complexity, 32 out of 7200 individuals (0.4%) from the final generation achieved the highest MI of 0.76. An analysis of these top-performing layouts reveals a clear design strategy that satisfies all five morphological requirements simultaneously. The exclusion of formal ordering rules results in visually irregular window arrangements. These outcomes demonstrate the framework's ability to emulate a design strategy of intentional asymmetry. The resulting façades are not merely irregular but exhibit composed arrangements. While not replicating the complex compositional hierarchy of specific architectural precedents, these arrangements can resonate with certain stylistic qualities, such as the deliberate asymmetry and varied fenestration seen in examples from Le Corbusier's Ronchamp Chapel (Ronchamp, France) to more contemporary designs (Fig. 17), thereby validating the framework's capacity to generate required morphologies.

The requirement for low balance is achieved through a pronounced asymmetric massing, where the majority of solid wall panels are concentrated on one side of the façade. This massing is pushed toward one of the vertical boundaries to satisfy the medium edge density rule, while the high continuity requirement ensures these panels form a large, connected surface. Accordingly, the resulting façades exhibit a strong duality: one side reads as a solid, heavy mass that dissolves into an open, transparent field on the other.

5.6. *Twin high-rise towers (DS5)*

The final case study, DS5, is designed as a definitive test of the framework's versatility and its capacity for nuanced stylistic control. This scenario conceptualizes a pair of 'twin' high-rise towers with distinct proportions: a tall, narrow tower (DS5a: 5 × 25) and a wider one (DS5b: 5 × 20). The core of this controlled experiment lies in its constraints: both towers are built from an identical, simple inventory of only solid and void panels ($t_{i,j} \in \{0, 1\}$) and are evaluated using the same set of seven morphological metrics. The only difference is related to the fuzzy rules, which convey two contrasting architectural philosophies. The first tower is guided by rules emphasizing a balanced, moderately dense composition with high continuity. The second is

Fig. 17. Kornerstone International Academy by hyperSity Architects photographed by Weiqi Jin in 2018 [76].

driven by a stricter logic prioritizing strong vertical symmetry and pattern repetition, while suppressing continuity.

The results of the optimization problem are illustrated in Fig. 18. The resulting façade layouts exemplify the divergence in the morphological expression. The first tall tower (Fig. 18(a)) exhibits a well-balanced and evenly distributed mass, resulting in a strong yet porous appearance with high carbon sequestration performance (e.g., −89.34 $\mathrm{tonCO_2e}$) due to the material density. The second tall tower (Fig. 18(c)) is characterized by a strong commitment to symmetry and structured repetition, which, combined with low continuity, produces a lighter, more open, and highly ordered composition. This comes at the cost of lower carbon sequestration (e.g., −39.84 $\mathrm{tonCO_2e}$).

The convergence plots in Fig. 18 also reveal the distinct paths taken to satisfy the design requirements. For the first tall tower, the MI rapidly converges to a high value of 0.87 (Fig. 18(b)). This is primarily driven by strong gains in the pattern, density, and balance metrics, which stabilize around generation 30. In sharp contrast, the second tall tower converges to a slightly lower MI of 0.84 (Fig. 18(d)), following a more volatile trajectory. Its optimization is dominated by a clear trade-off: vertical symmetry and pattern are maximized while continuity and edge density are suppressed. These distinct metric trajectories are a direct reflection of the different priorities imposed for each scenario.

5.7. AI-powered conceptual visualization

To demonstrate the visualization process, the methodology was applied to the two highest-ranked layouts from the DS5 case study (Figs. 18(a) and 18(c)). The translation was performed on June 12, 2025, using the LookX AI Cloud platform [63]. For each layout, the 2D grid served as the structural input, supplemented by a stylistic reference image available in LookX AI Cloud and a unique text prompt. To ensure the model respected the integrity of the input layouts while allowing for stylistic interpretation, the 'precise' render type was selected for both renderings. The text prompts were tailored to produce distinct architectural characters.

For the first concept (Fig. 19(a)), a descriptive, scene-based prompt was used: *"Modernist office building with multiple levels, utilizing concrete and glass materials. The architecture exudes modernity and futurism, suitable for high-tech companies or creative enterprises. Photorealistic, in an urban environment with surrounding activity, including pedestrians and vehicles"*. For the second tower (Fig. 19(b)), the prompt consisted of keywords referencing a specific architectural language: *"Distant shot, office building group, high rise, modern style, Mies van der Rohe, linear form, geometric form, glass curtain wall, marble, vertical frame, sunny, streets, landscape, commercial atmosphere"*.

The resulting renderings (Fig. 19) show how the model integrated the foundational grid of each layout with the specified stylistic cues. The process yielded distinct architectural concepts that adhere to the optimized patterns while being enriched with materiality and context. This final step illustrates how the framework's abstract outputs can be developed into detailed visual proposals, bridging the gap between computational analysis and design representation.

This visualization component is critical for the framework's real-world applicability in early conceptual design. By transforming abstract computational results into tangible, perceptible architectural concepts, it provides immediate feedback to designers, facilitating rapid stylistic iteration and the validation of optimized morphologies against a broader architectural vision. Moreover, these high-fidelity renderings serve as powerful communication tools, enabling architects to effectively convey design intent to clients and non-specialist stakeholders, thus ensuring that computationally generated solutions are both aesthetically compelling and practically understandable within a collaborative design process.

6. Conclusions

This research arises from the observation that, among the multiple characteristics of a building façade, morphology still lacks a systematic and operational way of being quantified in relation to explicitly stated design intentions. This gap limits the integration of morphological considerations into automated design and optimization processes, where morphology typically emerges as a byproduct rather than a controllable objective.

The main contribution of this paper is the formulation of a rigorous fuzzy logic-based methodology that translates high-level morphological preferences – expressed through customizable linguistic rules – into a quantitative measure, the Morphological Index (MI). A thought-provoking aspect of the present work is that the proposed methodology effectively enables designers to encode architectural intent directly into the optimization process, allowing morphology to be steered deliberately rather than implicitly. Across multiple scenarios, the conceptual design optimization identified solutions that reconciled competing morphological attributes in unexpectedly effective ways, underscoring the framework's capacity to reveal non-obvious design opportunities.

A sequence of numerical investigations of increasing complexity – ranging from controlled validation scenarios to a realistic twin-tower case study – demonstrated the versatility and reliability of the approach. In the latter, the workflow was further validated by translating optimized abstract grids into architectural concepts using AI-assisted rendering, showing that the optimized façades can be meaningfully interpreted at an architectural level.

The current framework is subject to some limitations. First, the formulation is two-dimensional and grid-based, an abstraction that offers computational tractability but does not yet represent volumetric interactions or the spatial depth of real façades. Second, the wall inventory and morphological metrics, while adaptable, remain abstractions of full architectural richness; surface attributes such as texture, color, or material transitions are not yet incorporated. Third, the fuzzy rule sets

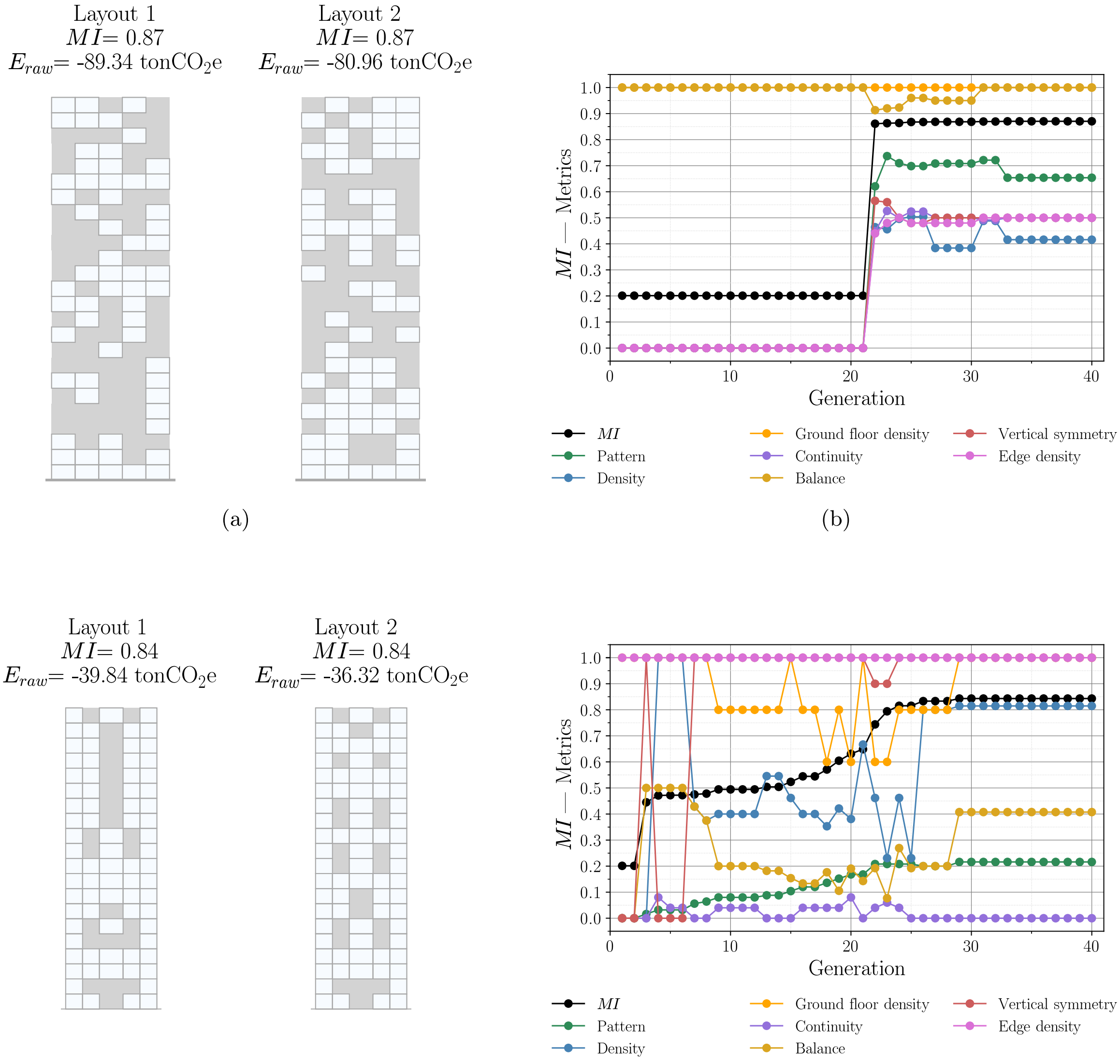

(a) (b) (c) (d)

Fig. 18. Two top-performing façade layouts and convergence behavior for design scenarios DS5a and DS5b: (a) and (c) show the highest-MI layouts while (b) and (d) illustrate the progression of the MI and contributing metrics over 40 generations.

(a) (b)

Fig. 19. AI-generated architectural visualizations of the two highest-ranked layouts for design scenario DS5: Layout 1 (a) and Layout 2 (b).

rely entirely on designer specification, which preserves interpretability but may require careful tuning for complex projects or large rule bases.

Building on these limitations, several promising avenues for future research can be identified.

- Extending the framework to three-dimensional façade geometries, which requires defining volumetric morphological metrics and expanding wall attributes to include depth, extrusions, recesses, and other spatial properties.
- Enriching the morphological vocabulary by incorporating additional surface-level attributes such as color, texture, or material transitions. Similarly, metrics linked to a façade's inner functional program or its relationship with the surrounding context can be developed.
- Developing mechanisms for semi-automatic calibration of fuzzy rule sets, combining designer input with data-driven or interactive learning approaches to enable more adaptive, iterative refinement.
- Embedding the MI into multi-objective optimization workflows that balance morphology with other performance criteria – such as daylight, energy, and embodied carbon – thus broadening applicability to later design stages.

CRediT authorship contribution statement

Carlotta Pia Contiguglia: Writing – original draft, Validation, Investigation, Data curation, Conceptualization. **Giuseppe Quaranta:** Writing – review & editing, Supervision, Software, Methodology, Investigation. **Cristoforo Demartino:** Writing – review & editing, Supervision, Resources, Project administration, Funding acquisition, Conceptualization. **Billie F. Spencer:** Writing – review & editing, Supervision, Methodology, Investigation.

Declaration of Generative AI and AI-assisted technologies in the writing process

During the preparation of this work, the authors used generative AI exclusively for grammar and language review. The scientific content, interpretations, and conclusions–as well as all data analysis–were produced by the authors, who take full responsibility for the integrity and accuracy of the published article.

Declaration of competing interest

The authors declare that they have no known competing financial interests or personal relationships that could have appeared to influence the work reported in this paper.

Acknowledgments

This study was carried out within the « Artificial Intelligence for ENVIronmental impact minimization of SEismic Retrofitting of Structures (AI-ENVISERS)» project – funded by European Union – Next Generation EU within the PRIN 2022 PNRR program (D.D.1409 del 14/09/2022 Ministero dell'Università e della Ricerca). This manuscript reflects only the authors' views and opinions, and the Ministry cannot be considered responsible for them.

Appendix A. Formulation of the morphological metrics

This appendix provides the detailed mathematical formulation for each of the morphological metrics summarized in Table 1. Each subsection is dedicated to a single metric and is structured to provide: (i) the underlying conceptual rationale, (ii) the complete mathematical formulation, and (iii) a set of simple, illustrative examples to aid interpretation. These examples are intentionally simplified using basic solid and void layouts to isolate and clarify the specific morphological characteristic that each metric is designed to quantify. Collectively, these formal definitions establish a rigorous numerical foundation upon which the FIS operates, translating the abstract qualities of façade design into computable inputs for the optimization framework.

A.1. Pattern

The pattern metric m_P is introduced to quantify the relative importance of recurring, uniform square or rectangular sub-patterns composed of identical wall types. It is calculated through sliding windows of varying size that scan the entire façade to identify both the existence and frequency of recurring sub-patterns. In particular, each window scans the block matrix representing the façade starting from the top-left corner and sliding horizontally and vertically across all possible positions. For each position, the fields of the façade within the window are then inspected to check whether they form a uniform square or rectangular block of identical non-empty wall types. Once such a sub-pattern is identified, the corresponding fields are marked to exclude them from overlapping regions of subsequent windows to prevent double-counting. Heights and widths of the moving windows are assigned a priori and collected in the set $\mathcal{W} = \{w\} = \left\{\left(w_H, w_L\right)\right\} = \left\{(1,2) \quad (1,3) \quad \cdots \quad (2,1) \quad (3,1) \quad \cdots \quad (M,N)\right\}$ (i.e., the size variables w_H and w_L represent the number of storeys and bays, respectively, of the moving window). For each window size $w = \left(w_H, w_L\right) \in \mathcal{W}$, a counting function $c_t(w)$ is then evaluated over all possible window positions. This function provides the number of occurrences of a sub-pattern of size $w \in \mathcal{W}$ composed entirely of a wall type $t \in \{\mathcal{T} \setminus 0\}$. The dominant sub-pattern is identified over the façade as the one corresponding to P_{max}, defined as follows:

$$P_{max} = \max_{t\in\{\mathcal{T}\setminus 0\}} \left(\max_{w\in\mathcal{W}} \left(w_H \cdot w_L \cdot c_t(w)\right)\right). \tag{A.1}$$

If the corresponding total number of filled fields in the façade is denoted as

$$F_{max} = \sum_{i=1}^{N} \sum_{j=1}^{M} 1_{\{t_{i,j}\neq 0\}}, \tag{A.2}$$

where $1_{\{\cdot\}}$ is a function that returns 1 if the condition given by $\{\cdot\}$ holds and 0 otherwise, then the pattern metric m_P is evaluated as follows:

$$m_P = \frac{P_{max}}{F_{max}}. \tag{A.3}$$

If a significant portion of the façade is composed of a single square or a rectangular repeating sub-pattern, this metric will yield a value closer to 1, indicating a strong and consistent repetitive visual appearance. Conversely, if the façade features minimal repetition and consists of diverse sub-patterns, the metric will produce a value closer to 0.

For example, consider the three façade layouts shown in Fig. A.20, each consisting of only a single wall type, where F_{max} is equal to 17, 16 and 18 for Figs. A.20(a), A.20(b) and A.20(c), respectively. For $w = (1,2)$, $c_T(1,2)$ is equal to 3, 4 and 2 for Figs. A.20(a), A.20(b) and A.20(c), respectively. The value of $c_T(2,1)$ corresponding to $w = (2,1)$ is also equal to 3 and 4 for Figs. A.20(a) and A.20(b), respectively, while it is 6 for Fig. A.20(c). If it is assumed $w = (1,3)$, then $c_T(1,3) = 1$ for all layouts but if a window size of $w = (3,1)$ is considered instead, $c_T(3,1)$ results equal to 1, 4 and 6 for Figs. A.20(a)–A.20(c), respectively. Moreover, it can be noted that it is possible to assume $w = (2,2)$ for Figs. A.20(b) and A.20(c) only, where $c_T(2,2) = 1$ for both, while $w = (3,3)$ as well as such that either w_H or w_L are larger than 3 are not feasible for all the layouts in Fig. A.20(a). This implies that the layout of Fig. A.20 leads to the lowest value of the pattern metric m_P since $P_{max} = 1 \cdot 2 \cdot 3 = 6$, corresponding to $w = (1,2)$, from which $m_P = 0.35$. The central layout of Fig. A.20(b) attains an intermediate value of the pattern metric m_P for $w = (3,1)$, with $P_{max} = 3 \cdot 1 \cdot 4 = 12$ corresponding to $m_P = 0.75$. The layout of the façade on the right achieves the maximum pattern metric score for $w = (3,1)$, as it leads $P_{max} = 3 \cdot 1 \cdot 6 = 18$, corresponding to $m_P = 1$.

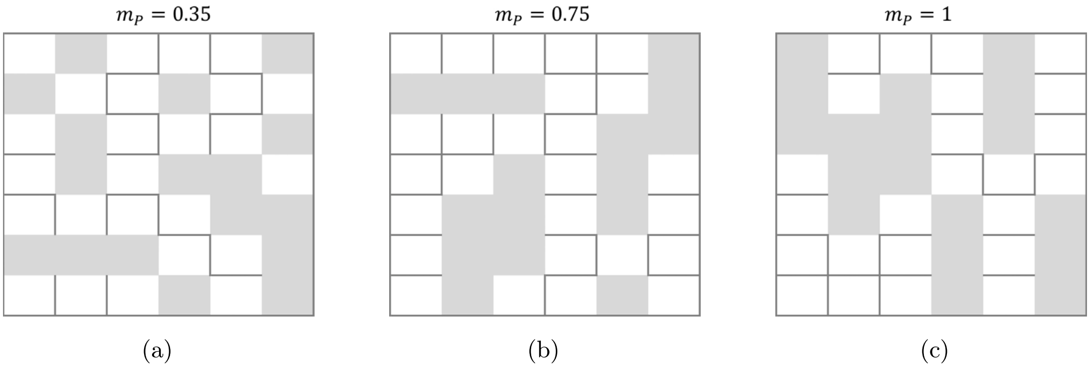

Fig. A.20. Illustration of the pattern metric m_P computed for three façade layouts with increasing regularity: (a) irregular layout with low pattern metric ($m_P = 0.35$); (b) intermediate regularity resulting in a higher pattern metric ($m_P = 0.75$); and (c) highly regular layout achieving the maximum pattern metric ($m_P = 1$).

A.2. Continuity

The continuity metric m_C evaluates the visual coherence of a building façade by detecting the largest connected paths of uniform wall type while considering its transparency. This accounts for the fact that walls with openings contribute less to the overall façade continuity compared to solid panels. The size of each connected portion is calculated using a depth-first search (DFS) type algorithm that recursively explores all neighboring fields with the same wall type, taking into account the transparency level. The pseudocode for this Depth-First Search (DFS) algorithm, which explicitly accounts for cell opaqueness during its recursive exploration, is provided in the Supplementary Material (Algorithm S3). Accordingly, the following index $DFS(i,j)$ is calculated for each (i,j)th field:

$$DFS(i,j) = \begin{cases} 0 & \text{if } V(i,j) = 1 \\ \rho(i,j) + \sum_{(i+d_i, j+d_j) \in \text{neighbors}(i,j)} \rho\left(i + d_i, j + d_j \mid t_{i+d_i, j+d_j} = t_{i,j}\right) & \text{otherwise} \end{cases} \tag{A.4}$$

Here, $V(i,j) = 1$ if the (i,j)th field has already been visited to avoid double counting whereas neighbors(i,j) represents the set of indices denoting the fields connected to the (i,j)th field (i.e., the fields that share at least one edge with another field). Herein, d_i and d_j are integer numbers that allow for indexing the fields connected to the (i,j)th field by moving in all orthogonal directions (i.e., up, down, left, or right). Moreover, $\rho(i,j)$ quantifies the contribution of the (i,j)th field as a function of its transparency level, assigning $\rho(i,j) = 1$ if the (i,j)th field consists of a solid panel, an intermediate value between 0 and 1 when an opening is present, and $\rho(i,j) = 0$ if the (i,j)th field is empty. For instance, $\rho(i,j)$ can be conveniently defined as the complementary value of the ratio of the opening area to the total area of the (i,j)th field. The largest connected path of fields is identified over the façade as the one corresponding to S_{max}, defined as follows:

$$S_{max} = \max_{\substack{1 \leq i \leq N \\ 1 \leq j \leq M}} \text{DFS}(i,j). \tag{A.5}$$

Finally, given the total number of fields F_{max} as per Eq. (A.2), the continuity metric m_C takes the following expression:

$$m_C = \frac{S_{max}}{F_{max}}. \tag{A.6}$$

This formulation allows for the quantification of the continuity in a way that accounts for the visual interruptions caused by openings, highlighting the contribution of solid, well-connected zones of the façade. A high value of m_C (close to 1) indicates that the largest connected zone makes up a significant portion of the filled fields. Conversely, a low value of m_C (closer to 0) suggests that the filled fields are fragmented into smaller, less connected portions.

For example, consider the three façade layouts shown in Fig. A.21, each consisting of only a single wall type. It is evident that $S_{max} = 1$ in Fig. A.21(a) as no field is connected to any other (i.e., no field shares an edge with another), and, since $F_{max} = 11$, $m_C = 1/11 = 0.09$. For Fig. A.21(b), each field is connected to no more than two other fields having the same wall type, and thus $S_{max} = 3$ and, for $F_{max} = 10$, it can be inferred that $m_C = 3/10 = 0.30$. Finally, each solid field in the layout of Fig. A.21(c) is connected to other 15 fields of the same type and then $S_{max} = 16$ from which, considering $F_{max} = 16$, it turns out that $m_C = 1$.

A.3. Symmetry

Symmetry is often a desirable feature in a rectangular or square façade and relates to its vertical axis, horizontal axis, or both. The symmetry of a façade depends on the arrangement of its panels, as a symmetrical façade features filled fields positioned symmetrically. Furthermore, the inherent geometry of the panels themselves is an important factor influencing the façade overall symmetry. For example, two walls on a façade placed symmetrically relative to the vertical axis and both featuring a centered square opening (e.g., a window) contribute positively to the overall vertical symmetry. Suppose these walls each have a lateral rectangular opening (e.g., a door). In that case, they also contribute positively to the vertical symmetry of the façade, provided the opening is left-sided on one wall and right-sided on the other. If this is not the case, a simple flipping operation along the vertical axis of one wall field may be sufficient to restore the overall vertical symmetry of the façade. However, there are instances where this flipping operation alone is inadequate to achieve full vertical symmetry.

With this premise, the vertical symmetry metric m_{S_V} is introduced to quantify the degree of symmetry of the façade relative to its vertical axis, defined as follows:

$$m_{S_V} = \frac{\sum_{i=1}^{N} \sum_{j=1}^{\left\lfloor \frac{M}{2} \right\rfloor} 1_{\{t_{i,j} = t_{i,M-j+1} \vee t_{i,j} = \text{flip}_V(t_{i,M-j+1}) \mid t_{i,j} \neq 0\}}}{\max\left(\sum_{i=1}^{N} \sum_{j=1}^{\left\lfloor \frac{M}{2} \right\rfloor} 1_{\{t_{i,j} \neq 0\}}, \sum_{i=1}^{N} \sum_{j=\left\lceil \frac{M}{2} \right\rceil}^{M} 1_{\{t_{i,j} \neq 0\}} \right)}. \tag{A.7}$$

where $\text{flip}_V(t)$ is the vertical flipping operator applied to a given wall type $t \in \mathcal{T}$ to produce its vertical mirrored layout. Similarly, the horizontal symmetry metric m_{S_H} is introduced to quantify the degree of symmetry of the façade relative to its horizontal axis, defined as

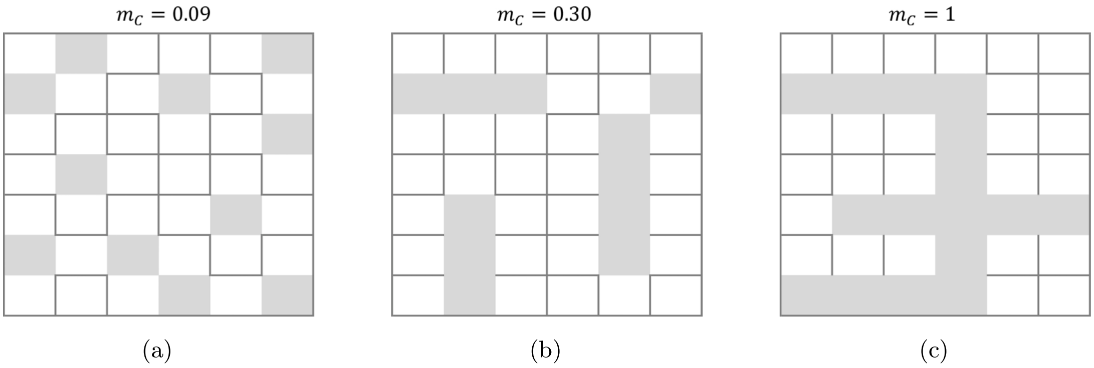

(a) (b) (c)

Fig. A.21. Illustration of the continuity metric m_C computed for three façade layouts exhibiting different degrees of visual coherence: (a) fragmented layout with minimal continuity ($m_C = 0.09$); (b) layout with moderate continuity ($m_C = 0.30$); and (c) highly continuous layout attaining the maximum continuity metric ($m_C = 1$).

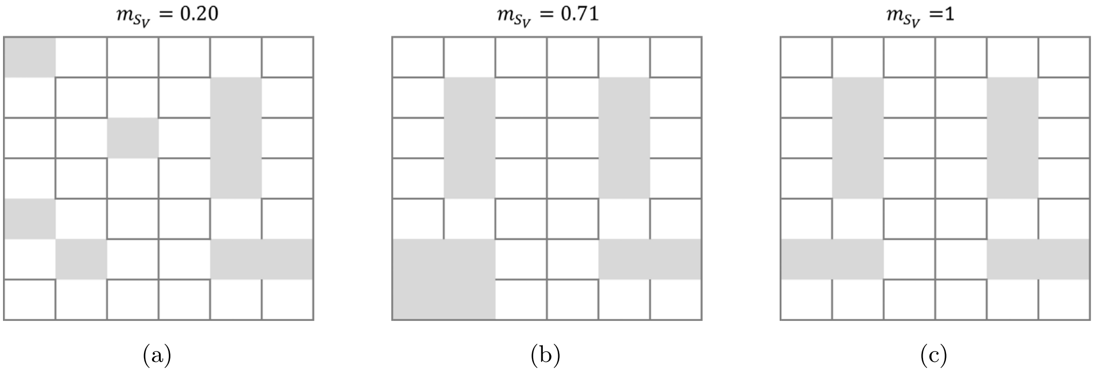

(a) (b) (c)

Fig. A.22. Illustration of the vertical symmetry metric m_{S_V} computed for three façade layouts with varying degrees of symmetry relative to their vertical axes: (a) asymmetric layout with minimal vertical symmetry ($m_{S_V} = 0.20$); (b) layout with partial vertical symmetry ($m_{S_V} = 0.71$); and (c) perfectly symmetrical layout attaining the maximum vertical symmetry ($m_{S_V} = 1$).

follows:

$$m_{S_H} = \frac{\sum_{i=1}^{\left\lfloor \frac{N}{2} \right\rfloor} \sum_{j=1}^{M} 1_{\{t_{i,j}=t_{N-i+1,j} \vee t_{i,j}=\mathrm{flip}_H(t_{N-i+1,j}) | t_{i,j}\neq 0\}}}{\max\left(\sum_{i=1}^{\left\lfloor \frac{N}{2} \right\rfloor} \sum_{j=1}^{M} 1_{\{t_{i,j}\neq 0\}}, \sum_{i=\left\lceil \frac{N}{2} \right\rceil}^{N} \sum_{j=1}^{M} 1_{\{t_{i,j}\neq 0\}} \right)}. \tag{A.8}$$

where $\mathrm{flip}_H(t)$ is the horizontal flipping operator applied to a given wall type $t \in \mathcal{T}$ to produce its horizontal mirrored layout.

Therefore, if the two vertical (horizontal) halves of the façade are mirror images of each other, possibly after applying a vertical (horizontal) flipping operation to some fields, then m_{S_V} (m_{S_H}) equals to 1. Conversely, when m_{S_V} (m_{S_H}) is close to 0, it indicates that either the walls are not positioned symmetrically relative to the vertical (horizontal) axis of the façade, or the vertical (horizontal) flipping operator is insufficient to restore the façade's vertical (horizontal) symmetry. It is noted that both horizontal and vertical symmetry are assumed to rely on wall positions and types, which implies that empty walls (i.e., $t_{i,j} = 0$) do not count toward m_{S_V} or m_{S_H}.

For instance, consider the three façade layouts shown in Fig. A.22, each consisting of only a single wall type. In Fig. A.22(a), the vertical symmetry condition for one half of the façade is satisfied by only one field out of 4 and 5 walls in the left and right vertical halves of the façade, resulting in $m_{S_V} = 1/5 = 0.20$. For the façade layout plotted in Fig. A.22(b), the vertical symmetry condition for one half of the façade is met by 5 walls in the left and right vertical halves, yielding $m_{S_V} = 5/7 = 0.71$. Finally, the perfect vertical symmetry of the façade layout in Fig. A.22(c) leads to $m_{S_V} = 5/5 = 1$.

Consider the three façade layouts shown in Fig. A.23, each consisting of only a single wall type. In Fig. A.23(a), the horizontal symmetry condition for one half of the façade is satisfied by two fields out of 4 and 6 walls in the lower and upper halves of the façade, resulting in $m_{S_H} = 2/6 = 0.33$. For the façade layout plotted in Fig. A.23(b), the horizontal symmetry condition for one half of the façade is met by 4 out of 6, yielding $m_{S_H} = 4/6 = 0.66$. Finally, the perfect horizontal symmetry of the façade layout in Fig. A.23(c) leads to $m_{S_H} = 8/8 = 1$.

A.4. Balance

The balance metric m_B measures the uniformity in the distribution of filled fields between the left and right halves of the façade. The contribution of each field to the façade balance is influenced by both transparency and size. For the left and the right half, the parameters B_L and B_R are first calculated:

$$B_L = \sum_{i=1}^{N} \sum_{j=1}^{\left\lfloor \frac{M}{2} \right\rfloor} \rho(i,j) \cdot L_j \cdot H_i, \tag{A.9}$$

$$B_R = \sum_{i=1}^{N} \sum_{j=\left\lceil \frac{M}{2} \right\rceil}^{M} \rho(i,j) \cdot L_j \cdot H_i. \tag{A.10}$$

Therefore, the balance metric m_B is determined as follows:

$$m_B = \frac{\min(B_L, B_R)}{\max(B_L, B_R)}. \tag{A.11}$$

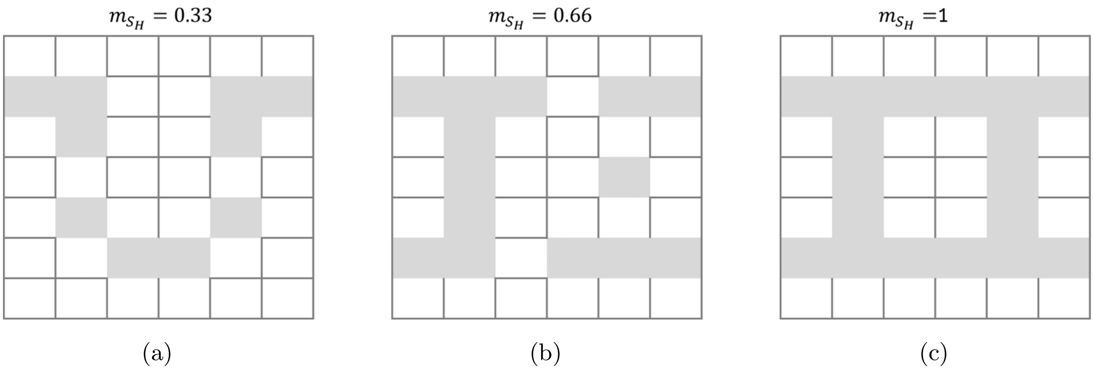

Fig. A.23. Illustration of the horizontal symmetry metric m_{S_H} computed for three façade layouts with varying degrees of symmetry relative to their horizontal axes: (a) asymmetric layout with minimal vertical symmetry ($m_{S_H} = 0.33$); (b) layout with partial vertical symmetry ($m_{S_H} = 0.66$); and (c) perfectly symmetrical layout attaining the maximum vertical symmetry ($m_{S_H} = 1$).

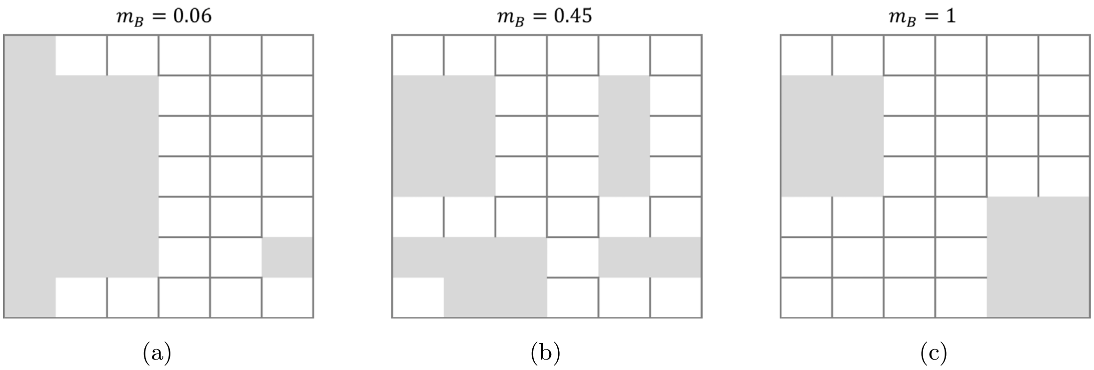

Fig. A.24. Illustration of the balance metric m_B computed for three façade layouts with different levels of uniformity in filled-field distribution between the left and right halves: (a) strongly unbalanced layout with most fields concentrated in one half ($m_B = 0.06$); (b) moderately balanced layout with partial unevenness in the distribution of fields ($m_B = 0.45$); and (c) perfectly balanced layout with equal distribution of fields between the façade halves, achieving the maximum balance metric ($m_B = 1$).

Balance metric m_B provides a value between 0 and 1, where $m_B = 1$ indicates perfect balance (i.e., filled fields are evenly distributed among the left and right halves of the façade) while $m_B = 0$ indicates maximum imbalance (i.e., filled fields are in only one half of the façade while the other half is empty).

For instance, consider the three façade layouts shown in Fig. A.24, each consisting of only a single wall type and assume that $L_j \cdot H_i = LH$ is constant. The layout in Fig. A.24(a) exhibits a strongly uneven distribution of filled fields, with $B_L = 17LH$ and $B_R = 1LH$, resulting in $m_B = 1/17 = 0.06$. The layout in Fig. A.24(b) shows a moderate imbalance of the filled fields between the two sides of the façade, with $B_L = 11LH$ and $B_R = 5LH$, and then $m_B = 5/11 = 0.45$. The layout in Fig. A.24(c) displays the best balance of the filled fields, which is confirmed by the fact that $B_L = B_R = 6LH$, corresponding to $m_B = 1$.

A.5. Rhythm

The rhythm metric m_R measures the extent to which a (non-empty) scheme of fields recurs periodically in the same positions across the storeys and bays of the façade. A 2-periodic scheme is considered, implying the search for a repeating scheme considering pairs of odd-indexed or even-indexed storeys or bays of the façade. Therefore, the following index is determined for the storeys, quantifying the number of odd-indexed and even-indexed storeys matching the target kth odd-indexed or even-indexed storey:

$$R_{storeys} = \frac{\max_{k\in\{a|a=2n-1\le N,n\in\{\mathbb{N}\setminus 0\}\}} \sum_{i=1}^{N} 1_{\{t_{2i-1,j}=t_{k,j}\ \forall j|\sum_{j=1}^{M} t_{k,j}\neq 0\}}}{N_a} + \frac{\max_{k\in\{b|b=2n\le N,n\in\{\mathbb{N}\setminus 0\}\}} \sum_{i=1}^{N} 1_{\{t_{2i,j}=t_{k,j}\ \forall j|\sum_{j=1}^{M} t_{k,j}\neq 0\}}}{N_b}, \quad (A.12)$$

where N_a and N_b are the number of odd-indexed and even-indexed storeys, respectively. A similar definition can be applied to quantify the rhythm of the bays. In this case, the following index is determined for the bays, quantifying the number of odd-indexed and even-indexed bays matching the target kth odd-indexed or even-indexed bay:

$$R_{bays} = \frac{\max_{k\in\{a|a=2n-1\le M,n\in\{\mathbb{N}\setminus 0\}\}} \sum_{j=1}^{M} 1_{\{t_{i,2j-1}=t_{i,k}\ \forall i|\sum_{i=1}^{N} t_{i,k}\neq 0\}}}{M_a} + \frac{\max_{k\in\{b|b=2n\le M,n\in\{\mathbb{N}\setminus 0\}\}} \sum_{j=1}^{M} 1_{\{t_{i,2j}=t_{i,k}\ \forall i|\sum_{i=1}^{N} t_{i,k}\neq 0\}}}{M_b}, \quad (A.13)$$

where M_a and M_b are the number of odd-indexed and even-indexed bays, respectively. Therefore, the rhythm metric m_R is determined as follows:

$$m_R = \frac{1}{2}\max(R_{storeys}, R_{bays}). \quad (A.14)$$

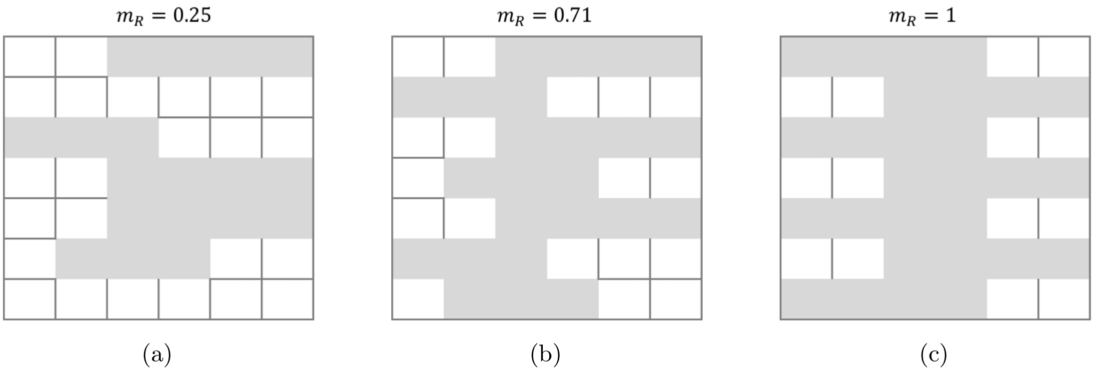

(a) (b) (c)

Fig. A.25. Illustration of the rhythm metric m_R computed for three façade layouts exhibiting different degrees of periodic repetition: (a) layout with limited rhythm and low periodic repetition ($m_R = 0.25$); (b) layout with moderate rhythm, partially recurring schemes across storeys or bays ($m_R = 0.71$); and (c) perfectly rhythmic layout, characterized by a fully periodic repetition of schemes across the façade, achieving the maximum rhythm metric ($m_R = 1$).

A value of m_R equal to 1 indicates high rhythm, meaning that all even-indexed storeys (or bays) are identical to each other, and all odd-indexed storeys (or bays) are identical to each other. On the other hand, if m_R tends to 0, then it indicates a deficiency of rhythm in the façade, meaning that there are no periodically repeating schemes neither in the storeys nor in the bays. Intermediate values between 0 and 1 reflect partial rhythm, where some but not all storeys or bays replicate the same scheme.

For instance, consider the three façade layouts in Fig. A.25, each consisting of only a single wall type. On one hand, for the layout depicted in Fig. A.25(a), it can be observed that a single scheme recurs only for two odd-indexed storeys of the façade, and thus $R_{storeys} = 2/4{+}0/3 = 0.5$ while $R_{bays} = 0$. On the other hand, for the layout shown in Fig. A.25(c), the odd-indexed and even-indexed storeys exhibit the same scheme, and thus $R_{storeys} = 4/4 + 3/3 = 2$ while $R_{bays} = 0$. Within the layout illustrated in Fig. A.25(b), one scheme recurs for two even-indexed storeys, whereas another scheme appears once for three odd-indexed storeys, and thus $R_{storeys} = 3/4{+}2/3 = 1.42$ while $R_{bays} = 0$. These observations are reflected in the values of m_R, which are 0.25, 0.71 and 1.00 for Figs. A.25(a), A.25(b), and A.25(c), respectively. This example also illustrates that a façade scoring well in terms of pattern may lack rhythm. For instance, while $m_P = 16/18 = 0.90$ for Fig. A.25(a) indicates a strong pattern score due to the high frequency of the occurrence of the sub-pattern $w = (2, 1)$, the value $m_R = 0.25$ highlights poor rhythm, attributable to the insufficient number of periodic repetitions of a given scheme.

A.6. Uniformity

The rhythm metric m_R establishes strict conditions on the spatial repetition of wall types across storeys and bays of the façade. To introduce a more flexible and type-agnostic approach, we define the uniformity metric m_U, which evaluates the evenness of wall presence without distinguishing between different types of walls. Unlike m_R, this metric focuses solely on the distribution density of non-empty fields ($t \neq 0$) across the façade grid, regardless of the specific wall type.

Let the binary indicator $B_{i,j}$ be 1 if the field at storey i and bay j contains any wall type ($t \neq 0$), and 0 otherwise. Define $M_i = \sum_{j=1}^{M} B_{i,j}$ as the number of wall-containing fields at storey i, and $M_j = \sum_{i=1}^{N} B_{i,j}$ as the number of wall-containing fields at bay j.

The standard deviations of the row and column distributions are then:

$$\sigma_{\text{storeys}} = \sqrt{\frac{1}{N}\sum_{i=1}^{N}\left(M_i - \mu_{\text{storeys}}\right)^2}, \quad \mu_{\text{storeys}} = \frac{1}{N}\sum_{i=1}^{N} M_i \tag{A.15}$$

$$\sigma_{\text{bays}} = \sqrt{\frac{1}{M}\sum_{j=1}^{M}\left(M_j - \mu_{\text{bays}}\right)^2}, \quad \mu_{\text{bays}} = \frac{1}{M}\sum_{j=1}^{M} M_j \tag{A.16}$$

These values capture the variation in the number of wall-containing fields along each axis. Maximum expected standard deviations occur when all walls are concentrated in a single row or column:

$$\sigma_{\text{storeys}}^{\max} = M\sqrt{\frac{1}{N}\left(1 - \frac{1}{N}\right)}, \quad \sigma_{\text{bays}}^{\max} = N\sqrt{\frac{1}{M}\left(1 - \frac{1}{M}\right)} \tag{A.17}$$

The uniformity metric is then computed as:

$$m_U = 1 - \frac{1}{2}\left(\frac{\sigma_{\text{storeys}}}{\sigma_{\text{storeys}}^{\max}} + \frac{\sigma_{\text{bays}}}{\sigma_{\text{bays}}^{\max}}\right) \tag{A.18}$$

Values of m_U close to 1 indicate a balanced and evenly populated façade, whereas lower values reflect clustering or voids, even when wall types vary.

For example, consider the three layouts in Fig. A.26, each with a binary distribution of filled (non-zero) and empty (zero) panels. Layout (a) concentrates walls in one storey, yielding low uniformity. Layout (b) spreads walls across rows but with some irregularities across columns, resulting in moderate uniformity. Finally, layout (c) achieves a more evenly filled distribution in both directions, leading to a high uniformity score.

The values of σ_{storeys} and σ_{bays} for Fig. A.26(a) are 2.25 and 0.5, respectively. In this layout, the low value of $m_U = 0.35$ indicates a highly non-uniform distribution. This outcome is mainly due to one storey being almost entirely filled, while others contain few or no filled fields. For the layout in Fig. A.26(b), the standard deviations are $\sigma_{\text{storeys}} = 0.64$ and $\sigma_{\text{bays}} = 1.10$. Here, the condition $\sigma_{\text{storeys}} < \sigma_{\text{bays}}$ suggests a greater variation across the bays than across the storeys. The resulting metric of $m_U = 0.64$ indicates moderate uniformity, reflecting a design that is quite regular horizontally but has a strong vertical stripe in one bay. Finally, for the layout in Fig. A.26(c), the standard deviations are $\sigma_{\text{storeys}} = 0$ and $\sigma_{\text{bays}} = 0.5$. The zero deviation for the storeys signifies a perfectly uniform vertical distribution. The value of $m_U = 0.90$ highlights the high overall uniformity of the façade, which is not a perfect 1.0 only because of the small remaining variation across the bays.

A.7. Density

The density metric m_D is introduced to quantify the overall transparency level of the façade. The effective contribution of each field is determined by its size and transparency level. The overall density metric m_D is then defined as the ratio of the total contribution of all

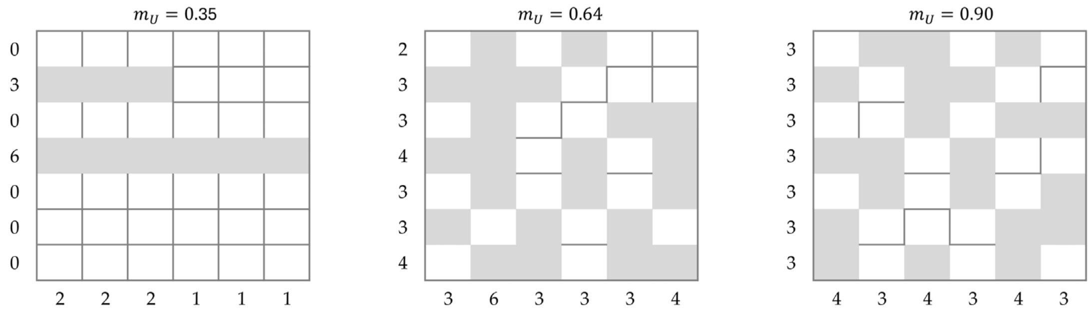

(a) (b) (c)

Fig. A.26. Illustration of the uniformity metric m_U computed for three façade layouts with increasing evenness in the distribution of wall elements: (a) clustered walls in one storey ($m_U = 0.35$); (b) more balanced with some irregularity ($m_U = 0.64$); (c) evenly spread across the grid ($m_U = 0.90$).

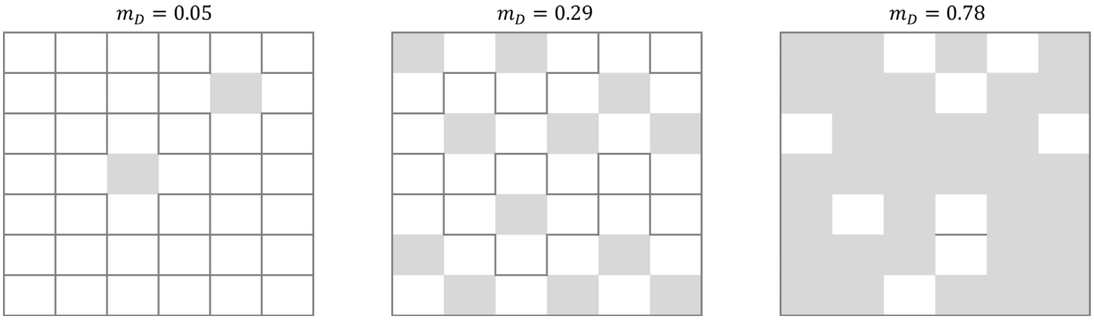

(a) (b) (c)

Fig. A.27. Illustration of the density metric m_D for three façade layouts exhibiting different levels of overall opacity: (a) predominantly transparent layout with few filled fields ($m_D = 0.05$); (b) moderately dense layout with more filled fields ($m_D = 0.29$); and (c) high-density layout featuring a large proportion of filled fields ($m_D = 0.78$).

fields in the façade to the maximum possible contribution, assuming all fields were fully opaque:

$$m_D = \frac{\sum_{i=1}^{N} \sum_{j=1}^{M} \rho(i,j) \cdot L_j \cdot H_i}{\sum_{i=1}^{N} \sum_{j=1}^{M} L_j \cdot H_i}, \tag{A.19}$$

yielding a value of m_D between 0 and 1, where $m_D = 1$ indicates a totally filled façade while $m_D = 0$ represents a completely transparent façade.

For instance, consider the three façade layouts in Fig. A.27, each consisting of only a single wall type and assume that $L_j \cdot H_i = LH$ is constant. The layout in Fig. A.27(a) corresponds to an almost fully transparent façade, as $m_D = 2/42 = 0.05$. The layout in Fig. A.27(b) shows a façade with rather low transparency level, as $m_D = 12/42 = 0.29$. The layout in Fig. A.27(c) displays a façade with a high filling ratio, corresponding to $m_D = 33/42 = 0.78$.

A.8. Ground floor density

The ground floor density metric m_G plays a key role in determining the transparency level at the base, which may be different from that of the overall façade. Specifically, the design can be possibly oriented toward a nearly filled façade where only the ground floor is transparent. To effectively achieve this goal in the façade design process, m_G is defined by taking into account the transparency level of the fields at the ground floor as follows:

$$m_G = \frac{\sum_{j=1}^{M} \rho(1,j)}{M}, \tag{A.20}$$

where M is the total number of fields at the ground floor. This metric reflects the filling rate of the ground floor of the façade, with $m_G = 0$ and $m_G = 1$ indicating empty and filled ground floor fields, respectively. It is noted that m_G is based solely on the transparency of the fields, as a distinct separation from the ground is expected to be visually apparent regardless of their size.

For instance, consider the three façade layouts in Fig. A.28, each consisting of only a single wall type and the same transparency level of the façade, except for the ground floor: in such cases, the value of m_G for Figs. A.28(a), A.28(b) and A.28(c) is equal to $1/6 = 0.17$, $4/6 = 0.67$, and $6/6 = 1$, respectively, reflecting a transition from a fully transparent to an almost fully opaque ground floor.

A.9. Edge density

The edge density metric m_E is considered to drive the design of the transparency level of the lateral bays of the façade. The design for transparency of the façade may be oriented toward opposite features, such as a façade that is nearly filled with only the lateral edges remaining transparent to distinctly separate it from adjacent constructions. In these design scenarios, the size of the lateral edge fields is irrelevant, while their level of transparency is crucial to ensure the required visual separation. The edge density metric is then estimated as follows:

$$m_E = \frac{\sum_{i=1}^{N} \rho(i,1) + \sum_{i=1}^{N} \rho(i,M)}{2N}, \tag{A.21}$$

where $2N$ is the total number of edge fields. This metric reflects the filling rate of the edges of the façade, with $m_E = 0$ and $m_E = 1$ indicating totally empty and filled edge fields, respectively.

For instance, consider the three façade layouts in Fig. A.29, each consisting of only a single wall type and the same transparency level of the façade, except for the lateral edges: the value of m_E for

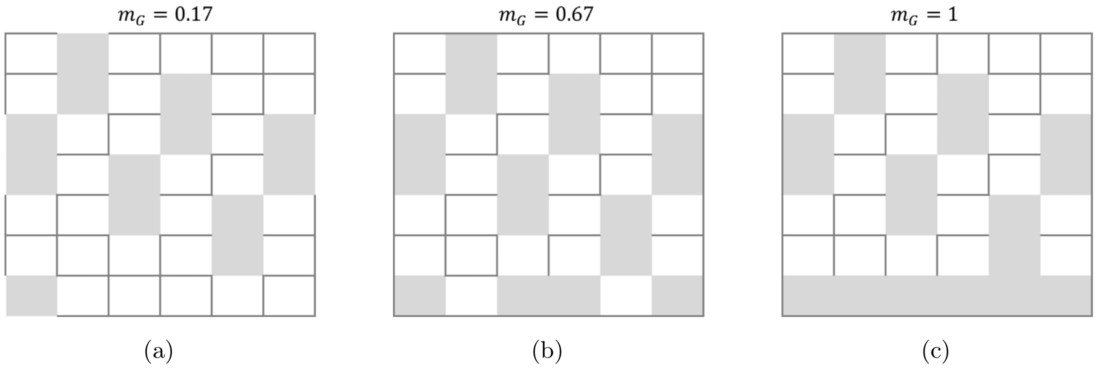

$m_G = 0.17$ $m_G = 0.67$ $m_G = 1$

(a) (b) (c)

Fig. A.28. Illustration of the ground floor density metric m_G for three façade layouts with different degrees of opacity at the base: (a) mostly transparent ground floor ($m_G = 0.17$); (b) partially filled ground floor ($m_G = 0.67$); and (c) fully opaque ground floor ($m_G = 1$).

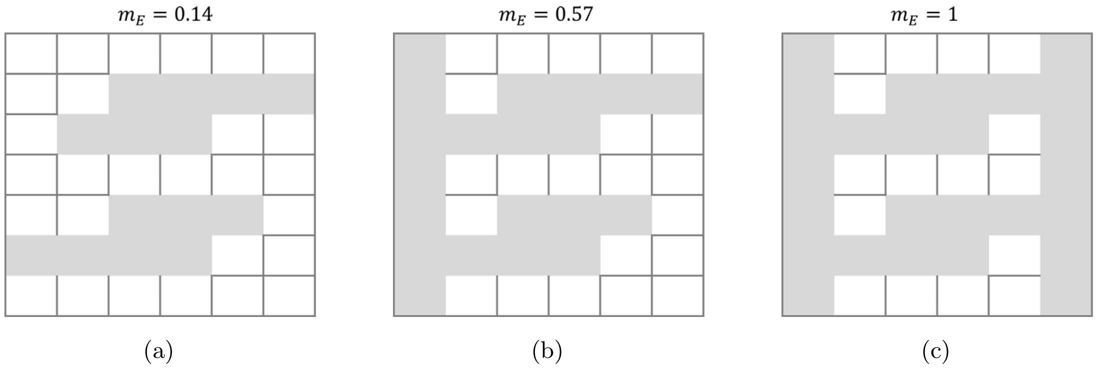

$m_E = 0.14$ $m_E = 0.57$ $m_E = 1$

(a) (b) (c)

Fig. A.29. Illustration of the edge density metric m_E for three façade layouts with different degrees of opacity along their lateral edges: (a) low edge density ($m_E = 0.14$), indicating mostly transparent edges; (b) moderate edge density ($m_E = 0.57$); and (c) fully opaque edges ($m_E = 1$).

Figs. A.29(a), A.29(b) and A.29(c) is equal to 0.14, 0.57, and 1, respectively, denoting a transition from almost fully transparent to fully opaque edges.

Appendix B. Supplementary data

Supplementary material related to this article can be found online at https://doi.org/10.1016/j.autcon.2025.106750.

Data availability

Data will be made available on request.

References

[1] J.A. Simpson, E.S.C. Weiner (Eds.), The Oxford English Dictionary, second ed., Oxford University Press, Oxford, UK, ISBN: 9780198611868, 1989.

[2] S. Moghtadernejad, M.S. Mirza, L.E. Chouinard, Façade design stages: Issues and considerations, J. Archit. Eng. 25 (1) (2019) 04018033, http://dx.doi.org/10.1061/(ASCE)AE.1943-5568.0000335, URL: https://ascelibrary.org/doi/abs/10.1061/%28ASCE%29AE.1943-5568.0000335.

[3] C. Cucuzzella, N. Rahimi, A. Soulikias, The evolution of the architectural façade since 1950: A contemporary categorization, Architecture 3 (1) (2023) 1–32, http://dx.doi.org/10.3390/architecture3010001, URL: https://www.mdpi.com/2673-8945/3/1/1.

[4] Online Etymology Dictionary, Morphology, 2023, URL: https://www.etymonline.com/word/morphology. (Accessed 26 February 2025).

[5] A. Prieto, M. Oldenhave, What makes a façade beautiful? architects' perspectives on the main aspects that inform aesthetic preferences in façade design, J. Facade Des. Eng. 9 (2) (2021) 21–46, http://dx.doi.org/10.7480/jfde.2021.2.5540, URL: https://jfde.eu/index.php/jfde/article/view/218.

[6] K. Kim, A. Luna-Navarro, J. Ciurlanti, S. Bianchi, A multi-criteria decision support framework for designing seismic and thermal resilient facades, Archit. Struct. Constr. 4 (2) (2024) 195–210, http://dx.doi.org/10.1007/s44150-024-00116-0, URL: https://link.springer.com/article/10.1007/s44150-024-00116-0.

[7] Z. Hu, T. Zayed, L. Cheng, A critical review of acoustic modeling and research on building façade, Build. Acoust. 29 (1) (2022) 107–134, http://dx.doi.org/10.1177/1351010X211022736.

[8] J.D. Silvestre, J.M.C.L. de Brito, M.G.C.A.D. Pinheiro, Sustainable building affordable to all, in: Portugal SB10 – Sustainable Building Affordable To All, Vilamoura, Portugal, ISBN: 978-989-96543-1-0, 2010, pp. 629–638.

[9] S. Lu, B. Lin, C. Wang, Investigation on the potential of improving daylight efficiency of office buildings by curved facade optimization, Build. Simul. 13 (2) (2020) 287–303, http://dx.doi.org/10.1007/s12273-019-0586-5.

[10] M. Saleem, G. Chhipi-Shrestha, M.T.B. Andrade, R. Dyck, R. Ruparathna, K. Hewage, R. Sadiq, Life cycle thinking–Based selection of building facades, J. Archit. Eng. 24 (4) (2018) 04018029, http://dx.doi.org/10.1061/(ASCE)AE.1943-5568.0000333, URL: https://ascelibrary.org/doi/abs/10.1061/%28ASCE%29AE.1943-5568.0000333.

[11] T. Herzog, R. Krippner, W. Lang, Facade Construction Manual, DETAIL – Institut für Internationale Architektur-Dokumentation GmbH & Co. KG, Munich, ISBN: 978-3-0346-1456-6, 2004, http://dx.doi.org/10.11129/detail.9783034614566, URL: https://doi.org/10.11129/detail.9783034614566.

[12] Z. Kuang, J. Zhang, Y. Li, T. Fukuda, Preserving architectural heritage in urban renewal: a stable diffusion model framework for automated historical facade generation, Npj Herit. Sci. 13 (1) (2025) 256, http://dx.doi.org/10.1038/s40494-025-01826-4.

[13] N. Gu, P. Amini Behbahani, A critical review of computational creativity in built environment design, Buildings 11 (1) (2021) http://dx.doi.org/10.3390/buildings11010029, URL: https://www.mdpi.com/2075-5309/11/1/29.

[14] A. Tabadkani, M. Valinejad Shoubi, F. Soflaei, S. Banihashemi, Integrated parametric design of adaptive facades for user's visual comfort, Autom. Constr. 106 (2019) 102857, http://dx.doi.org/10.1016/j.autcon.2019.102857, URL: https://www.sciencedirect.com/science/article/pii/S0926580518308240.

[15] W. Jabi, Parametric Design for Architecture, first ed., Laurence King Publishing, London, ISBN: 978-1780673141, 2013.

[16] G. Rapone, O. Saro, Optimisation of curtain wall façades for office buildings by means of PSO algorithm, Energy Build. 45 (2012) 189–196, http://dx.doi.org/

10.1016/j.enbuild.2011.11.003, URL: https://www.sciencedirect.com/science/article/pii/S0378778811005287.

[17] F. Bao, M. Schwarz, P. Wonka, Procedural facade variations from a single layout, ACM Trans. Graph. 32 (1) (2013) http://dx.doi.org/10.1145/2421636.2421644.

[18] R. Shan, L. Junghans, Multi-objective optimization for high-performance building facade design: A systematic literature review, Sustainability 15 (21) (2023) http://dx.doi.org/10.3390/su152115596, URL: https://www.mdpi.com/2071-1050/15/21/15596.

[19] S. Chang, D. Castro-Lacouture, Y. Yamagata, Decision support for retrofitting building envelopes using multi-objective optimization under uncertainties, J. Build. Eng. 32 (2020) 101413, http://dx.doi.org/10.1016/j.jobe.2020.101413, URL: https://www.sciencedirect.com/science/article/pii/S2352710219319825.

[20] Y. Shahbazi, M. Heydari, F. Haghparast, An early-stage design optimization for office buildings' façade providing high-energy performance and daylight, Indoor Built Environ. 28 (10) (2019) 1350–1367, http://dx.doi.org/10.1177/1420326X19840761.

[21] A. Elsheikh, I. Motawa, E. Diab, Multi-objective genetic algorithm optimization model for energy efficiency of residential building envelope under different climatic conditions in Egypt, Int. J. Constr. Manag. 23 (7) (2023) 1244–1253, http://dx.doi.org/10.1080/15623599.2021.1966709.

[22] Y.-H. Lin, M.-D. Lin, K.-T. Tsai, M.-J. Deng, H. Ishii, Multi-objective optimization design of green building envelopes and air conditioning systems for energy conservation and CO2 emission reduction, Sustain. Cities Soc. 64 (2021) 102555, http://dx.doi.org/10.1016/j.scs.2020.102555, URL: https://www.sciencedirect.com/science/article/pii/S2210670720307733.

[23] J. Gagne, M. Andersen, A generative facade design method based on daylighting performance goals, J. Build. Perform. Simul. 5 (3) (2012) 141–154, http://dx.doi.org/10.1080/19401493.2010.549572.

[24] Y.K. Yi, Building facade multi-objective optimization for daylight and aesthetical perception, Build. Environ. 156 (2019) 178–190, http://dx.doi.org/10.1016/j.buildenv.2019.04.002, URL: https://www.sciencedirect.com/science/article/pii/S0360132319302343.

[25] R.A. Rizi, A. Eltaweel, A user detective adaptive facade towards improving visual and thermal comfort, J. Build. Eng. 33 (2021) 101554, http://dx.doi.org/10.1016/j.jobe.2020.101554, URL: https://www.sciencedirect.com/science/article/pii/S2352710219329341.

[26] W. Yu, B. Li, H. Jia, M. Zhang, D. Wang, Application of multi-objective genetic algorithm to optimize energy efficiency and thermal comfort in building design, Energy Build. 88 (2015) 135–143, http://dx.doi.org/10.1016/j.enbuild.2014.11.063, URL: https://www.sciencedirect.com/science/article/pii/S0378778814010305.

[27] A. Pugnale, M. Sassone, Morphogenesis and structural optimization of shell structures with the aid of a genetic algorithm, in: M. Majowiecki (Ed.), Proceedings of the International Symposium of the International Association for Shell and Spatial Structures (IASS): Structural Architecture – Towards the Future Looking to the Past, International Association for Shell and Spatial Structures, Madrid, Spain, 2007, pp. 161–166, ISSN: 1028-365X.

[28] A. Gaspar-Cunha, D. Loyens, F. van Hattum, Aesthetic design using multi-objective evolutionary algorithms, in: R.H.C. Takahashi, K. Deb, E.F. Wanner, S. Greco (Eds.), Evolutionary Multi-Criterion Optimization, Springer Berlin Heidelberg, Berlin, Heidelberg, ISBN: 978-3-642-19893-9, 2011, pp. 374–388, http://dx.doi.org/10.1007/978-3-642-19893-9_26.

[29] J. Byrne, M. Fenton, E. Hemberg, J. McDermott, M. O'Neill, E. Shotton, C. Nally, Combining structural analysis and multi-objective criteria for evolutionary architectural design, in: Applications of Evolutionary Computation, Springer Berlin Heidelberg, Berlin, Heidelberg, ISBN: 978-3-642-20520-0, 2011, pp. 204–213, http://dx.doi.org/10.1007/978-3-642-20520-0_21, URL: http://dx.doi.org/10.1007/978-3-642-20520-0_21.

[30] G. Renner, A. Ekárt, Genetic algorithms in computer aided design, Comput. Aided Des. 35 (8) (2003) 709–726, http://dx.doi.org/10.1016/S0010-4485(03)00003-4, URL: https://www.sciencedirect.com/science/article/pii/S0010448503000034. Genetic Algorithms.

[31] L. Moreno-De-Luca, O.J.B. Carrillo, Multi-objective heuristic computation applied to architectural and structural design: A review, Int. J. Archit. Comput. 11 (4) (2013) 363–392, http://dx.doi.org/10.1260/1478-0771.11.4.363, arXiv:https://doi.org/10.1260/1478-0771.11.4.363.

[32] M.L. Castro Pena, A. Carballal, N. Rodríguez-Fernández, I. Santos, J. Romero, Artificial intelligence applied to conceptual design. A review of its use in architecture, Autom. Constr. 124 (2021) 103550, http://dx.doi.org/10.1016/j.autcon.2021.103550, URL: https://www.sciencedirect.com/science/article/pii/S0926580521000017.

[33] N. Rane, S. Choudhary, J. Rane, Leading-edge technologies for architectural design: a comprehensive review, SSRN Electron. J. (2023) http://dx.doi.org/10.2139/ssrn.4637891.

[34] N.K. Muthumanickam, N. Brown, J.P. Duarte, T.W. Simpson, Multidisciplinary design optimization in architecture, engineering, and construction: a detailed review and call for collaboration, Struct. Multidiscip. Optim. 66 (11) (2023) http://dx.doi.org/10.1007/s00158-023-03673-y, URL: https://www.osti.gov/biblio/2274791.

[35] E. Vissers-Similon, T. Dounas, J.D. Walsche, Classification of artificial intelligence techniques for early architectural design stages, Int. J. Archit. Comput. 23 (2) (2025) 387–404, http://dx.doi.org/10.1177/14780771241260857.

[36] A. Duran, C. Waibel, V. Piccioni, B. Bickel, A. Schlueter, A review on artificial intelligence applications for facades, Build. Environ. 269 (2025) 112310, http://dx.doi.org/10.1016/j.buildenv.2024.112310, URL: https://www.sciencedirect.com/science/article/pii/S0360132324011521.

[37] C. Li, T. Zhang, X. Du, Y. Zhang, H. Xie, Generative AI models for different steps in architectural design: A literature review, Front. Archit. Res. 14 (3) (2025) 759–783, http://dx.doi.org/10.1016/j.foar.2024.10.001, URL: https://www.sciencedirect.com/science/article/pii/S209526352400147X.

[38] K.S. Ochoa, P.O. Ohlbrock, P. D'Acunto, V. Moosavi, Beyond typologies, beyond optimization: Exploring novel structural forms at the interface of human and machine intelligence, Int. J. Archit. Comput. 19 (3) (2021) 466–490, http://dx.doi.org/10.1177/1478077120943062.

[39] Z. Guo, K. Saldana Ochoa, P. D'Acunto, Enhancing structural form-finding through a text-based AI engine coupled with computational graphic statics, in: Proceedings of IASS Annual Symposia, Vol. 2022, International Association for Shell and Spatial Structures (IASS), 2022, pp. 1–11, ISSN: 2518-6582.

[40] G. Klir, B. Yuan, Fuzzy Sets and Fuzzy Logic: Theory and Applications, Prentice Hall PTR, ISBN: 9780131011717, 1995, URL: https://books.google.it/books?id=AOhQAAAAMAAJ.

[41] L. Zadeh, R. Aliev, Fuzzy Logic Theory And Applications: Part I And Part II, World Scientific Publishing Company, ISBN: 9789813238190, 2018, URL: https://books.google.it/books?id=2PF9DwAAQBAJ.

[42] H. Zimmermann, Fuzzy Set Theory—and Its Applications, SpringerLink : Bücher, Springer Netherlands, ISBN: 9789401006460, 2011, URL: https://books.google.it/books?id=HVHtCAAAQBAJ.

[43] Fuzzy Thinking: The New Science of Fuzzy Logic, Flamingo, 1994, URL: https://books.google.it/books?id=TBmvQgAACAAJ.

[44] B.C. Arabacioglu, Using fuzzy inference system for architectural space analysis, Appl. Soft. Comput. 10 (3) (2010) 926–937, http://dx.doi.org/10.1016/j.asoc.2009.10.011, URL: https://www.sciencedirect.com/science/article/pii/S1568494609002014.

[45] A. Mars, E. Grabska, G. Ślusarczyk, B. Strug, Design characteristics and aesthetics in evolutionary design of architectural forms directed by fuzzy evaluation, Artif. Intell. Eng. Des. Anal. Manuf. 34 (2) (2020) 147–159, http://dx.doi.org/10.1017/S0890060420000153.

[46] J. Buckley, E. Eslami, An Introduction to Fuzzy Logic and Fuzzy Sets, Advances in Intelligent and Soft Computing, Physica-Verlag HD, ISBN: 9783790814477, 2002, URL: https://link.springer.com/book/10.1007/978-3-7908-1799-7.

[47] R. Seising, M. Tabacchi, A very brief history of soft computing: Fuzzy sets, artificial neural networks and evolutionary computation, 2013, pp. 739–744, http://dx.doi.org/10.1109/IFSA-NAFIPS.2013.6608492.

[48] L. Zadeh, Fuzzy sets as a basis for a theory of possibility, Fuzzy Sets and Systems 100 (1999) 9–34, http://dx.doi.org/10.1016/S0165-0114(99)80004-9, URL: https://www.sciencedirect.com/science/article/pii/S0165011499800049.

[49] B. Tepavčević, V. Stojaković, Procedural modeling in architecture based on statistical and fuzzy inference, Autom. Constr. 35 (2013) 329–337, http://dx.doi.org/10.1016/j.autcon.2013.05.015, URL: https://www.sciencedirect.com/science/article/pii/S0926580513000824.

[50] S. Cafiso, R. Lamm, G.L. Cava, Fuzzy model for safety evaluation process of new and old roads, Transp. Res. Rec. 1881 (1) (2004) 54–62, http://dx.doi.org/10.3141/1881-07.

[51] E. Wehrle, M. Wedekind, H. Baier, Fuzzy modeling of imprecise material parameters in the analysis of metal matrix composite structures, in: ASME 2011 International Mechanical Engineering Congress and Exposition, IMECE 2011, Vol. 9, 2011, http://dx.doi.org/10.1115/IMECE2011-63794.

[52] A.S. Hanna, W.B. Lotfallah, A fuzzy logic approach to the selection of cranes, Autom. Constr. 8 (5) (1999) 597–608, http://dx.doi.org/10.1016/S0926-5805(99)00009-6, URL: https://www.sciencedirect.com/science/article/pii/S0926580599000096.

[53] E. Pourjavad, A. Shahin, The application of mamdani fuzzy inference system in evaluating green supply chain management performance, Int. J. Fuzzy Syst. 20 (3) (2018) 901–912, http://dx.doi.org/10.1007/s40815-017-0378-y.

[54] Mamdani, Application of fuzzy logic to approximate reasoning using linguistic synthesis, IEEE Trans. Comput. C-26 (12) (1977) 1182–1191, http://dx.doi.org/10.1109/TC.1977.1674779.

[55] M. Sugeno, T. Yasukawa, A fuzzy-logic-based approach to qualitative modeling, IEEE Trans. Fuzzy Syst. 1 (1) (1993) 7, http://dx.doi.org/10.1109/TFUZZ.1993.390281.

[56] D. Dubois, H. Prade, What are fuzzy rules and how to use them, Fuzzy Sets and Systems 84 (2) (1996) 169–185, http://dx.doi.org/10.1016/0165-0114(96)00066-8, URL: https://www.sciencedirect.com/science/article/pii/0165011496000668.

[57] J. Mendel, Fuzzy logic systems for engineering: a tutorial, Proc. IEEE 83 (3) (1995) 345–377, http://dx.doi.org/10.1109/5.364485.

[58] J. Wang, S. Han, X. Li, 3D fuzzy ergonomic analysis for rapid workplace design and modification in construction, Autom. Constr. 123 (2021) 103521, http://dx.doi.org/10.1016/j.autcon.2020.103521, URL: https://www.sciencedirect.com/science/article/pii/S0926580520311018.

[59] G.C. Marano, G. Quaranta, M. Mezzina, Fuzzy time-dependent reliability analysis of RC beams subject to pitting corrosion, J. Mater. Civ. Eng. 20 (9) (2008) 578–587, http://dx.doi.org/10.1061/(ASCE)0899-1561(2008)20:9(578), URL: https://ascelibrary.org/doi/abs/10.1061/%28ASCE%290899-1561%282008%2920%3A9%28578%29.

[60] X.-S. Yang, Nature-Inspired Optimization Algorithms, Elsevier, London, 2014, http://dx.doi.org/10.1016/C2013-0-01368-0.

[61] A. Konak, D.W. Coit, A.E. Smith, Multi-objective optimization using genetic algorithms: A tutorial, Reliab. Eng. Syst. Saf. 91 (9) (2006) 992–1007, http://dx.doi.org/10.1016/j.ress.2005.11.018, URL: https://www.sciencedirect.com/science/article/pii/S0951832005002012.

[62] Y. Yılmaz, B. Çiğdem Yılmaz, A weighted multi-objective optimisation approach to improve based facade aperture sizes in terms of energy, thermal comfort and daylight usage, J. Build. Phys. 44 (5) (2021) 435–460, http://dx.doi.org/10.1177/1744259120930047.

[63] LookX, Lookx AI cloud platform, 2025, URL: https://www.lookx.ai. (Accessed 22 June 2025).

[64] J.D. Warner, scikit-fuzzy team, Scikit-fuzzy, 2019, URL: http://github.com/scikit-fuzzy/scikit-fuzzy. Version 0.4.2.

[65] J. Blank, K. Deb, Pymoo: Multi-objective optimization in Python, IEEE Access 8 (2020) 89497–89509, http://dx.doi.org/10.1109/ACCESS.2020.2990567.

[66] K.A.D. Jong, W.M. Spears, A formal analysis of the role of multi-point crossover in genetic algorithms, Ann. Math. Artif. Intell. 5 (1) (1992) 1–26, http://dx.doi.org/10.1007/BF01530777.

[67] K. Deb, R.B. Agrawal, Simulated binary crossover for continuous search space, Complex Systems 9 (2) (1995) 115–148, URL: https://www.complex-systems.com/abstracts/v09_i02_a02/.

[68] K. Deb, Multi-objective optimisation using evolutionary algorithms: An introduction, in: L. Wang, A.H.C. Ng, K. Deb (Eds.), Multi-Objective Evolutionary Optimisation for Product Design and Manufacturing, Springer London, London, 2011, pp. 3–34, http://dx.doi.org/10.1007/978-0-85729-652-8_1.

[69] S. Salcedo-Sanz, A survey of repair methods used as constraint handling techniques in evolutionary algorithms, Comput. Sci. Rev. 3 (3) (2009) 175–192, http://dx.doi.org/10.1016/j.cosrev.2009.07.001, URL: https://www.sciencedirect.com/science/article/pii/S1574013709000379.

[70] Y.J. Cao, Q.H. Wu, D.W. Shimmin, Study of initial population in evolutionary programming, in: 1997 European Control Conference, ECC, 1997, pp. 1394–1397, http://dx.doi.org/10.23919/ECC.1997.7082295.

[71] H. Maaranen, K. Miettinen, M. Mäkelä, Quasi-random initial population for genetic algorithms, Comput. Math. Appl. 47 (12) (2004) 1885–1895, http://dx.doi.org/10.1016/j.camwa.2003.07.011, URL: https://www.sciencedirect.com/science/article/pii/S0898122104840240.

[72] M.A. Navarro, D. Oliva, A. Ramos-Michel, B. Morales-Castañeda, D. Zaldívar, A. Luque-Chang, A review of the use of quasi-random number generators to initialize the population in Meta-Heuristic algorithms, Arch. Comput. Methods Eng. 29 (7) (2022) 5149–5184, http://dx.doi.org/10.1007/s11831-022-09759-y.

[73] Rubner, Cross laminated timber update, 2023, URL: https://www.rubner.com/wp-content/uploads/2023/07/cross-laminated-timber-update-1.pdf. (Accessed 20 March 2025).

[74] Institut Bauen und Umwelt e.V. (IBU), Environmental product declarations (EPD), 2025, URL: https://ibu-epd.com/en. (Accessed 20 March 2025).

[75] Alphacan SRL, Environmental product declaration: Extreme section – PVC window 1.23 m × 1.48 m, Environmental Product Declaration EPDITALY0509, EPDItaly, 2023, URL: https://www.epditaly.it/epd/extreme-section-pvc-window-123m-x-148m/. Version 1.0. Valid until 2025-06-01. (Accessed 12 February 2025).

[76] W. Jin, Photograph of Kindergarten in Yinchuan by hyperStiy Architects, 2018, URL: https://www.archdaily.com/904798/kornerstone-international-academy-hyperstiy-architects. (Accessed 10 July 2025).